Reply to the comments by L. Shao

We appreciate the valuable comments.

Comment (1) This manuscript presented a number of mineral species according to the elemental compositions obtained by the TEM-EDXS. However, minerals have general characteristics of 'isomorphism' or 'polymorphism', so we cannot classify the particle mineralogy merely according to the elemental compositions of particles. In this manuscript, the authors have referred to the XRD results and have also used the selected area electronic diffraction as well as lattice fringe imaging. Although these methods of mineral identification was introduced in Jeong and Nousiainen (2014), it is necessary to have a simple description of how to interpret mineral species according to EDXP patterns in this current manuscript.

Reply (1) The procedures of mineral identification using EDXS, lattice fringe imaging, and electron diffraction are now provided in the supplement information. We agree that mineral identification should be conservative because of isomorphism or polymorphism. It is impossible to identify all the minerals on the species level. Identification of calcite, dolomite, and quartz are straightforward on the basis of TEM-EDXS spectra. However, we cannot separately identify three $KAlSi_3O_8$ polymorph mineral species including sanidine, orthoclase, and microcline soley on the basis of TEM-EDXS pattern. Even the lattice fringe imaging and electron diffraction pattern are not straightforward to polymorph identification because of the similar crystal structures. Since the purpose of our study is not in-depth crystal-structural study of each mineral, we group three $KAlSi_3O_8$ polymorphs into K-feldspar. Chlorite and plagioclase are also mineral groups but not species. Without the aid of electron diffraction and lattice fringe imaging, we can identify plagioclase based on TEM-EDXS spectra easily, but the identification of plagioclase mineral species including albite, oligoclase, andesine,... is not straightforward because we have to know the accurate ratio of Ca and Na. Frequent Na loss during the TEM operation and FIB sample preparation inhibits the precise determination of plagioclase chemical composition. Identification of nano-thin illite, smectite, illite-smectite mixed layers is also challenging as discussed in the text and Jeong and Nousiainen (2014), resulting in grouping them into illite-smectite series clay minerals (ISCMs). Although TEM is a powerful tool for the identification of fine mineral grains in the dust particles in comparison to SEM and XRD, identification is limited in many cases because of beam damage and high vacuum.

Changes in the manuscript (1) The procedures of mineral identification using EDXS, lattice fringe imaging, and electron diffraction are **now provided in the supplement information as attached at the end of this letter**.

Comment (2) Page 9 section'3.6 Comparison with single-particle properties of Asian dust is interesting to see that cay minerals are predominant minerals in the Sahara dust storm particles. This is different from the Asian Dust Storm (ADS) samples and I guess this is mainly due to differences in the particle sizes. Please refer to the paper on the mineralogy of the ADS dust fall and PM10 samples, in which quartz occupied a predominant position (Shao et al., 2007, ADVANCES IN ATMOSPHERIC SCIENCES, VOL. 25, NO. 3, 2008, 395-403). Please check if there are any variations of mineral types in association with the particle sizes between Sahara dust and Asian dust storm particles. Plus, the size-segregated mineral compositions may be more important in characterizing mineralogical properties.

Reply (2) We agree that mineralogical properties are related to the particle size. We hope to analyze coarse particles of Saharan dust (> 10 μm) by XRD and SEM in future if samples are available. Our study was focused on the clarification of the internal structures and mineralogy of Saharan dust

particles. In the original manuscript, we presented the mineral composition of total dust particles from two impact stages. Table 1 was revised by adding the mineral compositions of two impact stages (0.9–2.6 μm and > 2.6 μm) as shown below. Dust particles of the two size fractions were dominated by clay minerals including ISCMs and kaolinite. Dust particles of 0.9–2.6 μm in size, however, were slightly enriched with clay minerals in comparison with those of > 2.6 μm in size, while coarser particles (> 2.6 μm) were rather enriched with non-clay minerals including quartz, plagioclase, and K-feldspar.

Changes in the manuscript (2) We changed the first paragraph of the section 2 Samples and methods to **"**Dust samples used in this study collected from the top of the tower building of the meteorological observatory of Izaña, Tenerife, Spain (28° 18' 33.8" N, 16° 29' 56.9" W, 2395 m a.s.l.). Details on the procedure and location can be found in Kandler et al. (2007). Particles were collected with a cascade impactor on carbon adhesive, with nominal stage size ranges of > 2.6 μm, 0.9–2.6 μm, and 0.1–0.9 μm (50 % efficiency cut-off aerodynamical particle diameter), of which the stages with > 0.9 μm were used for analysis. All samples were stored in a desiccator under dry conditions prior to analysis. The sample analyzed in the present work was collected during a 10 min period on 15 July 2005 at 09:33 h (UTC). It was selected as best-representing the campaign to achieve the greatest atmospheric relevance. Its composition is close to the mean campaign composition (cf. Kandler et al., 2007, Fig. 8), and the corresponding transport trajectory is central in the observed trajectory field (Fig. 1 and Kandler et al., 2007, Fig. 9). According to AERONET aerosol optical thickness data (Supplement Fig. 1), the concentration on the sampling day was also close to the average of the dust event lasting from July 12 to July 22, 2005. Analysis was limited to particles with diameter < 5 μm, as too few larger ones were available**"**

SEM-EDXS results of two impact stages were added to Table 1.

Table 1. Mineral number % of Saharan dust based on SEM-EDXS analyses of single particles.

Size	No. of particle	Total clay minerals	ISCMs*	Ka	Ch	Bt	Q	P	Kf	Am	Ca	D	Fe	Ti	Gy	Sp	Ap
Saharan dust, Tenerife (This study)																	
0.9-2.5 μm	*n*=1191	1005	868	131	6	0	105	21	17	1	12	5	8	8	9	0	0
	%	84.4	72.9	11.0	0.5	0.0	8.8	1.8	1.4	0.1	1.0	0.4	0.7	0.7	0.8	0.0	0.0
> 2.5 μm	*n*=435	314	260	45	8	1	59	23	17	1	9	1	3	2	4	1	1
	%	72.7	60.2	10.4	1.9	0.2	13.7	5.3	3.9	0.2	2.1	0.2	0.7	0.5	0.9	0.2	0.2
Total	*n*=1626	1319	1128	176	14	1	164	44	34	2	21	6	11	10	13	1	1
	%	81.1	69.4	10.8	0.9	0.1	10.1	2.7	2.1	0.1	1.3	0.4	0.7	0.6	0.8	0.1	0.1
Asian dust, Korea (Jeong and Achterberg, 2014)**																	
%		56.1	48.4	1.8	3.9	2.1	18.7	10.5	4.0	0.7	6.5	1.0	1.2	0.2	0.8	0.2	0.2

*ISCM=illite-smectite series clay minerals, Ka=kaolinite, Ch=chlorite, Bt=biotite, Q=quartz, P=plagioclase, Kf=K-feldspar, Am=amphibole, Ca=calcite, D=dolomite, Fe=iron (hydr)oxide, Ti=Ti oxide, Gy=gypsum, Sp=sphene, Ap=apatite.

** Average value of the SEM-EDXS results from three Asian dust samples presented in Jeong and Achterberg (2014). Vaules are slightly differernt from those in Jeong and Achterberg (2014) by the change of mineral species considered for quantification.

We added and revised Section 3.1 Mineral composition of bulk dust: "Single-particle SEM-EDXS data showed that dust particles in both size fractions were dominated by clay minerals including ISCMs and kaolinite. Dust particles of 0.9–2.6 μm in size, however, were slightly enriched in clay minerals in comparison with those of > 2.6 μm in size, while non-clay minerals including quartz, plagioclase, and K-feldspar were rather enriched in coarser particles (> 2.6 μm). Average mineral composition was ISCMs 69%, kaolinite 11%, quartz 10%, plagioclase 3%, K-feldspar 2%, calcite 1%, chlorite 1%, iron (hydr)oxide 1%, titanium oxide 1%, and gypsum 1% (Table 1). The total clay

mineral content was 81%."
We added sentences to the section 3.6 Comparison with single-particle properties of Asian dust: "Previous data showed that total clay content of Saharan dust ranged from 61% to 73% in the samples of the Atlantic islands (Glaccum and Prospero,1980), from 56% to 81% in the dustfall collected in Spain (Avila et al., 1997), and around 81% in two Saharan dust samples collected in Cape Verde (Jeong and Achterberg, 2014). Total clay content of Asian dust ranged from 28% to 50% in Beijing, China (Shao et al., 2008) and around 57% in Korea (Jeong and Achterberg, 2014). Thus, clay minerals are likely enriched in Saharan dust in comparison with Asian dust."
Shao et al. (2007) was added to the list of reference.

Comment (3) Page 6, '3.2 Internal structures of individual dust particles': When discussing the internal structures of individual dust particles, 'Clay-rich particles', 'Large minerals with clay-rich coatings', 'Intergrade particles': : :.., were classified. I am wondering if the term 'aggregate' may be more suitable for these particle categories since the particles presented in this current manuscript are actually the aggregates of minerals, i.e., rock fragments. Not necessary secondary coating.

Reply (3) Our manuscript was written assuming readers majorly working in the fields of atmospheric chemistry, environment, and light scattering where mineral dusts are treated as airborne 'particles' of ranging sizes and mineralogy. Of course, the particles are agglomerates (or aggregates) of smaller mineral grains. In the text an individual airborne solid object was termed "particle" and a particle constituent was termed "grain" (so particles are agglomerates of small mineral grains).

Changes in the manuscript (3) We would like to keep the term 'particle'.

Comment (4) Section "Samples and methods": The methodology needs to be introduced in more detail. A total of 1626 individual particles were analyzed, but how many samples were analyzed? How do you select particles on the filter? Are these samples representative of typical peak dust storm episodes or a non-storm episodes? A table of sample information may be useful.

Reply (4) One dust sample during a dusty period lasting from July 12th to July 22nd, 2005 (Kandler et al., 2007) was analyzed in this study. There was no local aerosol concentration measurement, but according to data available from AERONET and WDCA, the day of sampling (July 15th, 2005) had an average AOT. The sample was selected to be closest to the campaign composition average and the central transport trajectory. This is described in the modified manuscript now. So, the sample can be regarded as representative for a medium intensity dust event.

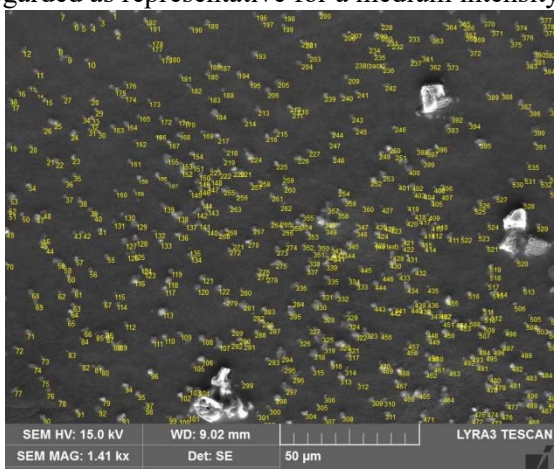

0.9 – 2.6 µm size fraction

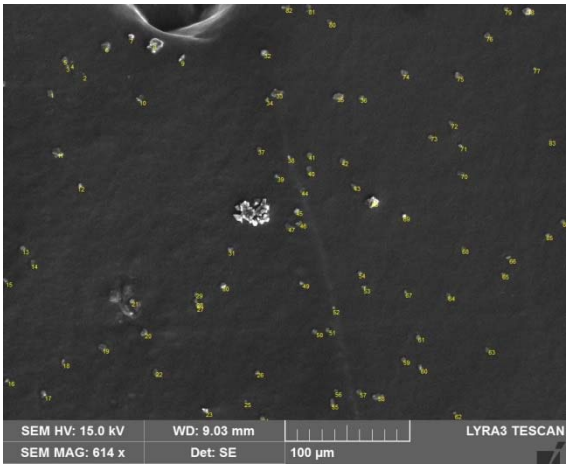

> 2.6 µm size fraction

For SEM-EDXS analyses, we selected rectangular areas where dust particles were homogeneously distributed as shown in two SEM images above. Then, we analyzed all the particles within the area. We have analyzed 1191 and 435 dust particles from impact stage 0.9–2.6 μm and > 2.6 μm, respectively. Total number of analyzed particles was 1626. We have presented the SEM-EDXS result of total 1626 dust particles in the Table 1 of original manuscript. We added SEM-EDXS results of two impact stages to the revised Table 1 as shown above. The data show that fine dust particles were more enriched in clays.
Since FIB slicing cannot be applied to all the particles, 21 and 27 dust particles were selected for FIB work from the size ranges of 0.9–2.6 μm and > 2.6 μm, respectively. Dust particles for FIB work was selected to reflect the mineral abundance of the bulk dust determined by SEM-EDXS single particle analyses. Thus, we think that the internal structures found in this study are representative of the dust particles. The experimental section was revised to clarify particle selection.

Changes in the manuscript (4) We added to the revised manuscript a plot on aerosol optical thickness of July 2005 to Supplement Fig. 1.

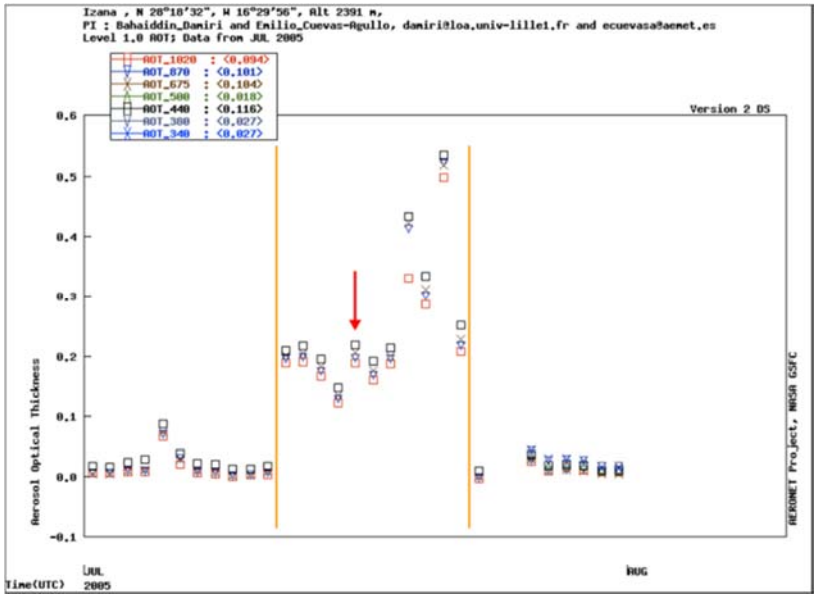

Supplement Fig. 1: Aerosol Robotic Network aerosol optical thickness for Izana, July 2005. Begin and end of the July dust period is marked by orange bars, the sampling day is indicated by a red arrow. Figure created by http://aeronet.gsfc.nasa.gov/cgi-bin/bamgomas_interactive on September 6th, 2016.

We added two paragraphs to the section 2 Samples and Methods:
"All the particles collected on the impact stages were not analyzed. We selected rectangular areas of homogeneous particle distribution at low magnification, and then, EDXS patterns were obtained from all the particles in the areas. Total number of the analyzed dust particles was 1626: 1191 particles from the impact stage 0.9–2.6 μm, and 435 particles from the stage > 2.6 μm)."
"The mineral composition obtained by this method is evidently semi-quantitative, considering large inherent uncertainty. Previous analyses of Asian dust, however, showed that SEM-EDXS results were consistent with XRD results (Park and Jeong, 2016). The 48 target particles for FIB work were selected according to the mineralogical types of the dust particles, reflecting mineral abundance of bulk dust determined by EDXS analyses: 21 particles from the impact stage 0.9–2.6 μm and 27 particles from the impact stage > 2.6 μm, respectively."

Comment (5) The total clay content determined by XRD for the Cape Verde dust sample was 81%, matching the proportion obtained using single-particle SEM-EDXS data in this study. The value '81%'

is a sme value for two cases, too precise!. The XRD measured the volume or weight percentages while the EDXS give a number percentages, and two methods will not give the same results. Please check this carefully.

Reply (5) Dust samples for TEM and SEM analyses in this study were collected in the Tenerife, Canary Islands. Thus, complete matching between XRD data of Cape Verde dust and SEM data Tenerife dust is impossible, and only accidental. Close matching of analytical values of two dust samples support the reliability of our XRD and SEM-EDXS quantification procedure applied to minute dust samples. Nevertheless both data are incomplete because of the lack of either XRD or SEM-EDXS data. This has been caused by unavailability of samples suitable for XRD in Tenerife and SEM-EDXS single particle analysis in Cape Verde (sampling campaign were done several years ago).

Changes in the manuscript (5) Thus, we deleted the comparison of Tenerife SEM-EDXS data to Cape Verde XRD data.

Comment (6) Page 21, Fig.2c, the ‘kaolin’ might be ‘kaolinite’?

Reply and Changes in the manuscript (6) The ‘kaolin’ in Fig.2c was replaced by ‘kaolinite’ in the revised version.

Supplement Information will be included in the revised manuscript.

Supplement Information – Mineral identification

Minerals have their own crystal structures and chemical compositions. Thus, mineral identification using TEM is based on the lattice-fringe imaging and electron diffraction providing structural information and EDXS providing chemical information. Precise identification of all the minerals in the FIB slice to the species level is practically impossible because of beam damage, high vacuum, lower reliability of lattice fringes/electron diffraction data in comparison with XRD, and enormous time required.

TEM identification of nonphyllosilicate minerals

The identification of quartz, K-feldspar, plagioclase, calcite, amphibole, dolomite, titanite, apatite, and gypsum was straightforward based on their characteristic EDX spectra (Fig. S1). Although we could not identify mineral species of K-feldspar (sanidine, orthoclase, microcline), plagioclase (albite, oligoclase, andesine...), and amphibole (tremolite, actinolite, hornblende...) using time-consuming complex operation, the purpose of current mineral dust research was satisfied by grouping similar mineral species. Silica phase of the mineral dust from desert was almost quartz, consistent with XRD although few amorphous silica was identified by electron diffraction.

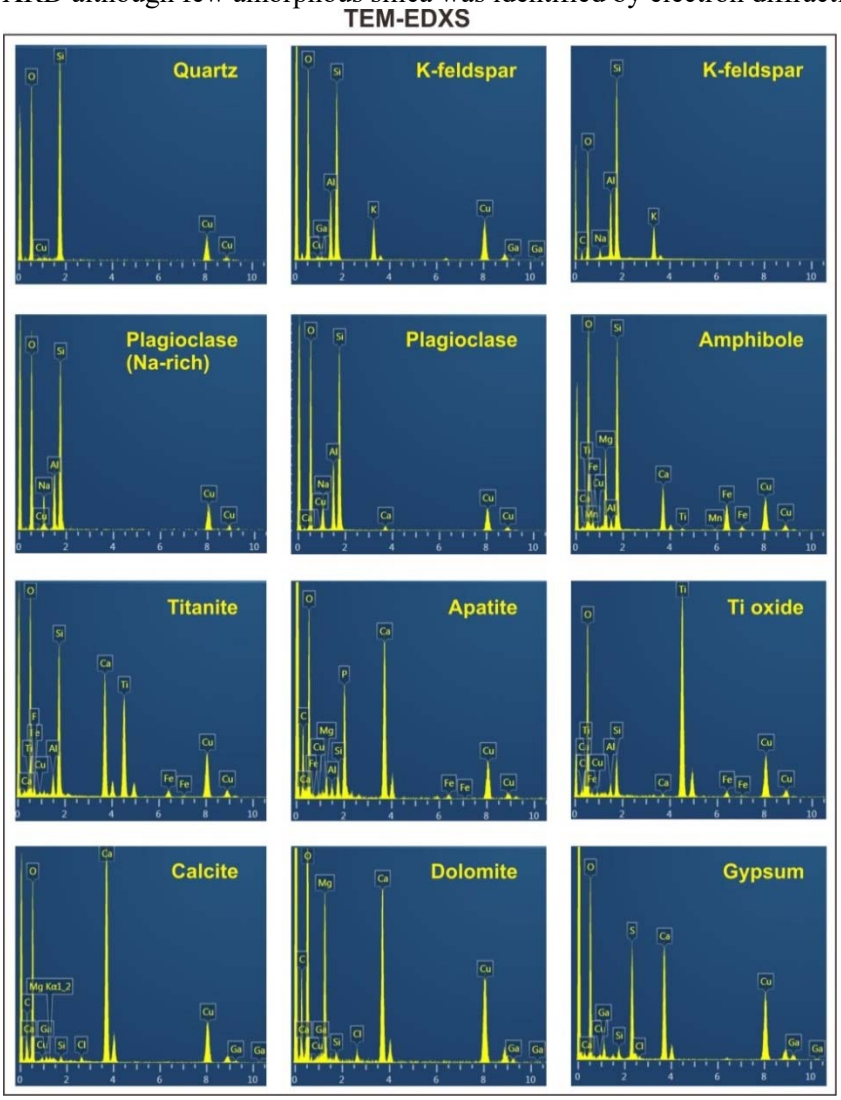

Fig. S1. TEM EDXS patterns of constituent minerals of dust particles obtained from the cross-sectional slices prepared by FIB.

TEM identification of phyllosilicate minerals

Phyllosilicate minerals were abundant in the mineral dust. The identification of muscovite, biotite, and chlorite was rather straightforward from their characteristic chemical compositions with the aid of lattice-fringe imaging (Fig. S2). However, the identification of nano-thin phyllosilicates (clay minerals) was difficult because of their breakdown under electron beam and small grain size below the minimum diameter of electron beam for EDXS. They occurred often as agglomerates. In addition, mixed layering of illite and smectite is common in natural soils. The identification of clay minerals was based on lattice fringes and chemical compositions: 1.0 nm for illite, ~1.0 nm for smectite and vermiculite, and ~7.0 nm for kaolinite (Fig. S2). Kaolinite was directly identified from its EDXS with the aid of lattice fringe imaging. However, illite, smectite, and illite-smectite mixed layers could not be separately identified each other because smectite was contracted under the high vacuum of the TEM chamber, showing ~1.0 nm lattice fringes similar to those of illite. Although EDXS can be used for identifying illite and smectite with interlayer cations K and Ca, respectively, they cannot be separately analyzed using EDXS, even when using an electron beam as small as possible. Therefore, we could not distinguish between nano-thin illite, smectite, and their mixed-layers, using conventional TEM work. To avoid over-interpretation, nano-thin platelets of clay minerals showing ~1.0 nm lattice fringes with varying K and Ca contents were grouped into illite-smectite series clay minerals (ISCMs). ISCMs are nano-scale mixtures of nano-thin platelets of illite, smectite, and illite-smectite mixed-layers.

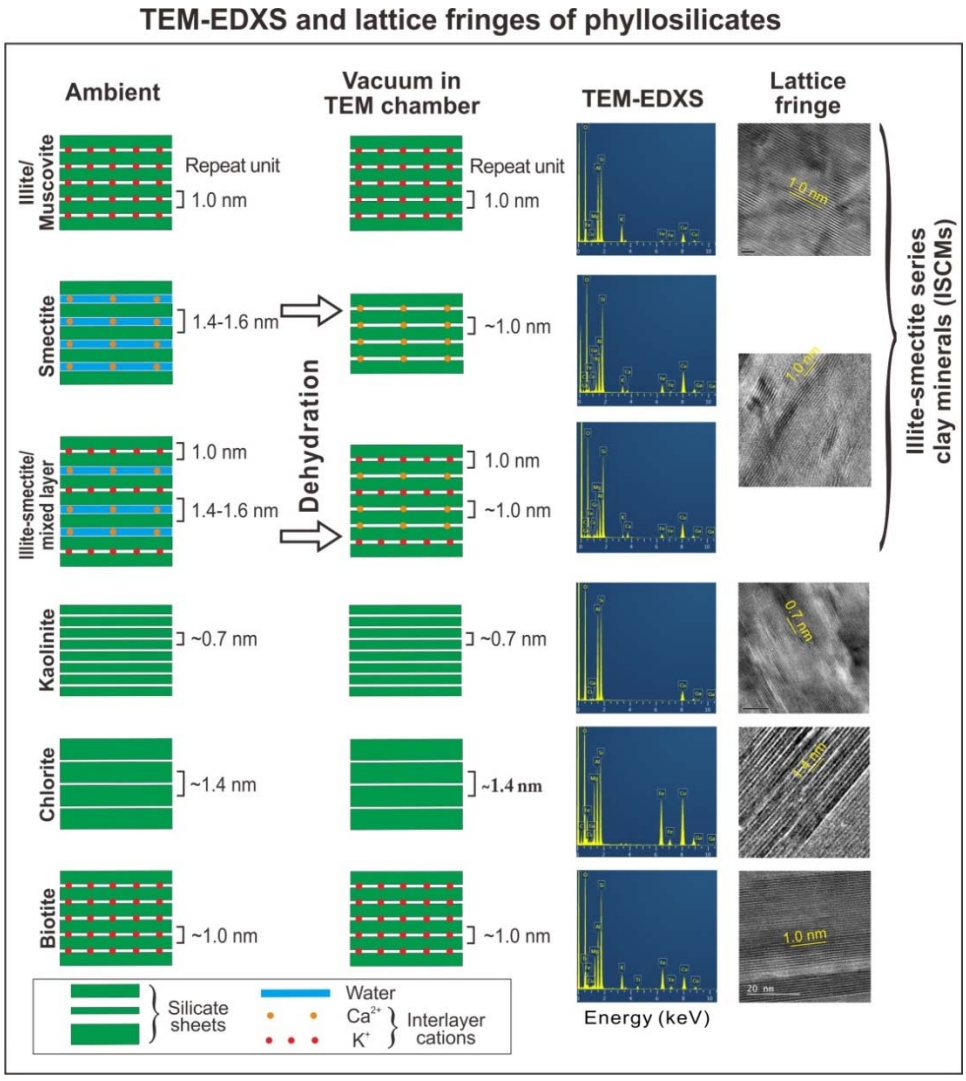

Fig. S2. Identification of phyllosilicates using TEM-EDXS and lattice fringes.

TEM identification of iron (hydr)oxides

Mineralogical identification of iron (hydr)oxides was also challenging. EDXS could not be used for the identification. Electron diffraction and lattice-fringe imaging should be used in combination as shown in Fig. S3. However, many iron (hydr)oxide grains could not be identified because of the overlap of many *d*-spacings, varying crystallographic orientation, and tiny grain sizes. Thus, we used species names only in cases in which mineral species were identified unambiguously by lattice fringe imaging and electron diffraction; in other cases, we used the collective term "iron (hydr)oxide".

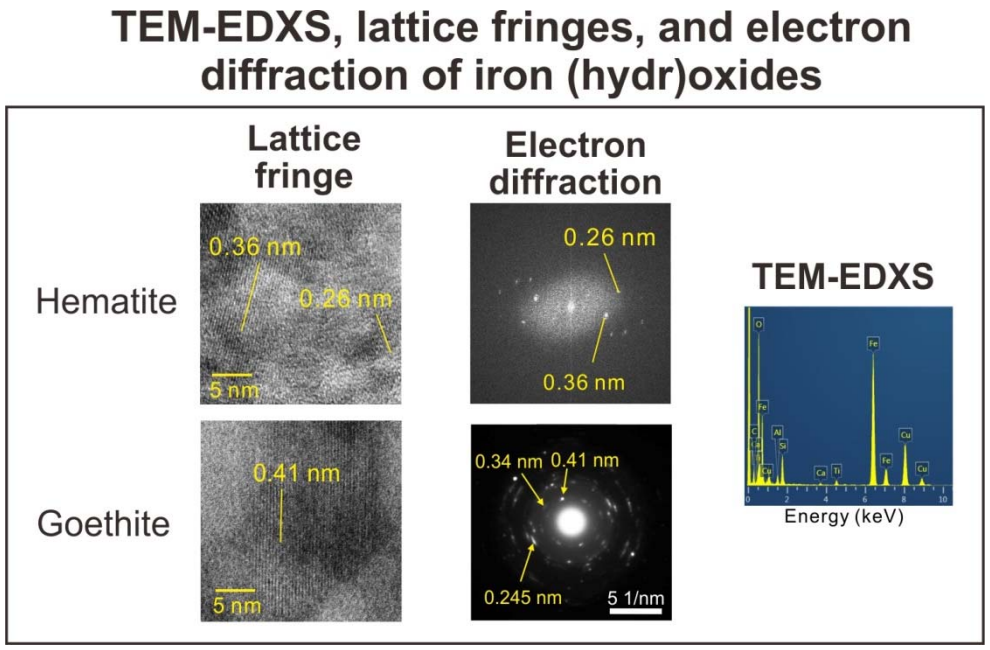

Fig. S3. Identification of phyllosilicates using lattice fringes and electron diffraction.

Mineralogical classification of dust particles using SEM-EDXS

Dust particles are essentially mixtures of mineral grains of diverse species and sizes. In case the quantity of powder dust samples is sufficient (~several hundred mg), XRD method is best for the determination of mineral composition. SEM-EDXS analyses of individual particle can be used when powder samples are insufficient or non-available. Ideally, mineral composition of individual dust particle can be determined by mixing several minerals to get the overall chemical composition of the particle. Then, the summation of the mineral compositions of thousands of dust particles considering their volume would lead to the mineral composition of bulk dust. However, the irregular morphology of dust particles prohibits the accurate determination of dust particles due to the difficulty of calibration. In addition, the chemical compositions of constituent minerals are varied. Prior to the development of reliable quantitative analysis procedure based on SEM for the mineral composition of individual dust particle, we adopted semi-quantitative approach. Since dust particles are generally dominated by one mineral species or group, we have determined the predominant mineral of a dust particle referring to the EDXS patterns of pure minerals as shown in Figs. S1 and S2. In case particles show intermediate EDXS pattern (Fig. S4), half of the particle was counted (0.5). Summation of the counts led to the approximate mineral composition of bulk dust. Although the procedure is evidently semi-quantitative, SEM-EDXS results were consistent with XRD results in the recent analyses of Asian dust (Table 1 in Park and Jeong (2016), Journal of the Mineralogical Society of Korea, 29, 79–87).

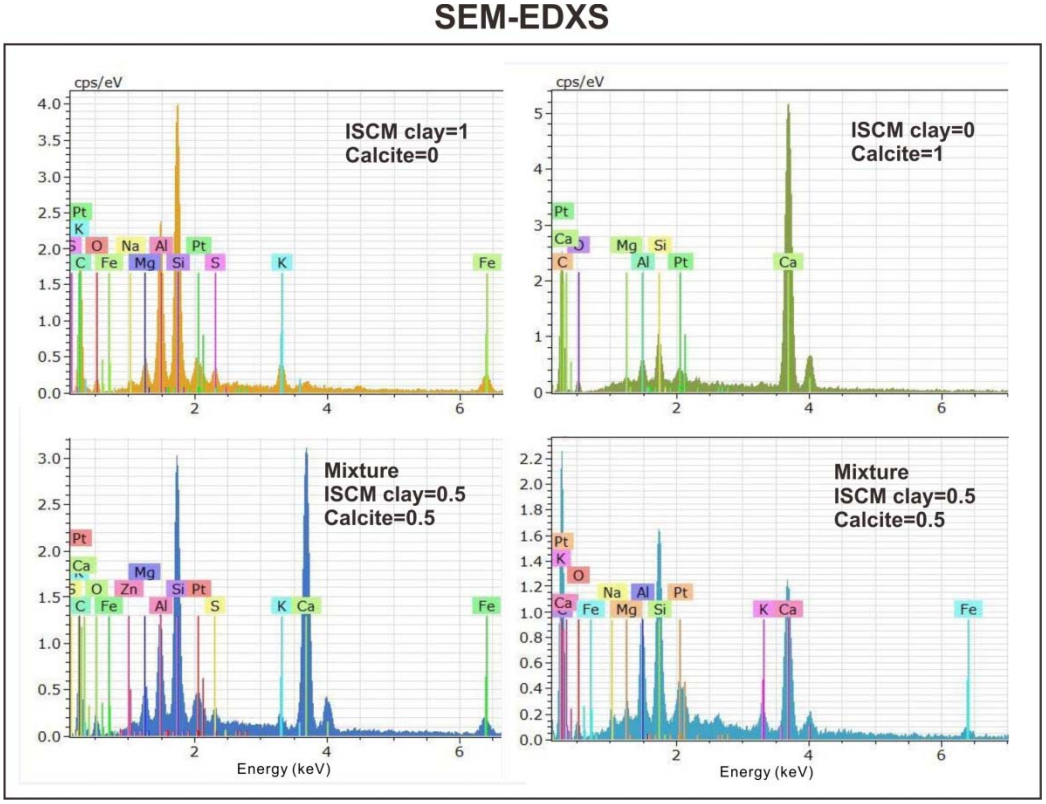

Fig. S4. SEM-EDXS of dust particles.

Park and Jeong (2016)

Table 1. Mineral compositions of Asian dusts determined by XRD analysis and SEM-EDS single particle analysis

Minerals	Asian dust XRD				
	Feb 22 2015	Mar 18 2014	Mar 31 2012	Mar 20 2010	Average
	(This study)	(Jeong and Achterberg, 2014)			
ISCMs	55	60	42	50	51
Kaolinite	2	1	3	4	3
Chlorite	5	3	6	7	5
Total clay	*62*	*64*	*52*	*61*	59
Quartz	18	14	23	15	17
Plagioclase	10	11	15	10	12
K-feldspar	4	0	6	2	3
Amphibole	0	0	1	2	1
Calcite	5	5	2	5	4
Gypsum	1	6	2	6	4
Total	100	100	100	100	100
	SEM single particle analysis				
ISCMs	57	54	48	54	52
Kaolinite	2	1	3	2	2
Chlorite	3	2	4	6	4
Total clay	*62*	*58*	*55*	*62*	58
Quartz	19	19	21	17	19
Plagioclase	9	11	11	10	11
K-feldspar	3	4	5	3	4
Amphibole	0	1	1	0	1
Calcite	4	7	7	6	7
Gypsum	2	0	1	1	1
Total	100	100	100	100	100

We will prepare final version considering comment and reply above.

Sincerely

On behalf of co-authors

Gi Young Jeong
Corresponding Author

Reply to the comments by Karine Deboudt

We appreciate the valuable comments.

Comment (1) Several samples were collected, but considering the technical difficulties for sample preparation, one sample was only studied for its mineralogical properties and internal structures (collected the 15 July 2005 at 9:33). How was it chosen among all samples? Which impaction stages were selected? Why? What was the PM2.5 concentration during sampling? It should be more precisely exposed in the "sample and methods" part.

Reply (1) The sample was chosen due to its closeness to the campaign average in terms of composition and trajectories. Particles were analyzed from the super-micron impaction stages, as they are most complex with respect to optical properties. We have added the corresponding description to the manuscript. Mass concentrations are unfortunately not available for the campaign, but AOT data from aerosol and WDCA shows that the sample was taken during a medium AOT.

Changes in manuscript (1) Corresponding information is provided in the supplement Fig. 1.

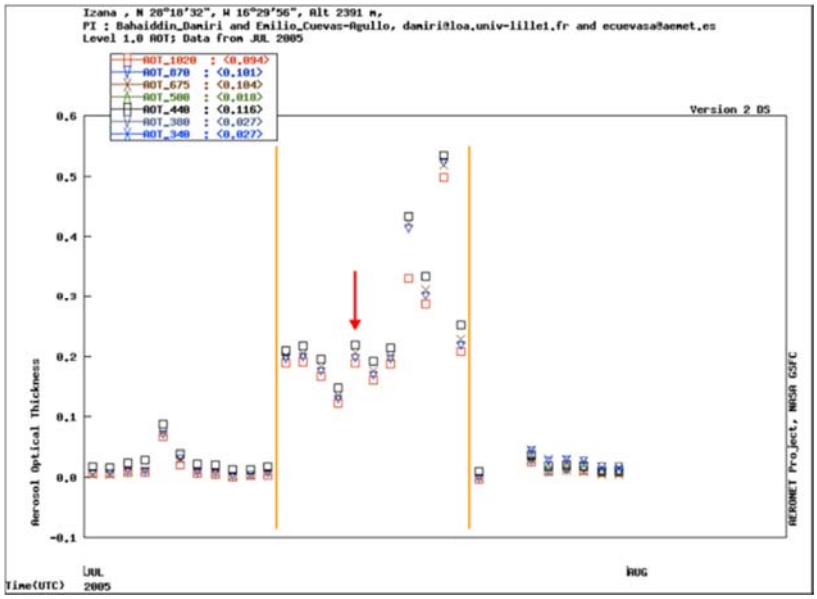

Supplement Fig. 1: Aerosol Robotic Network aerosol optical thickness for Izana, July 2005. Begin and end of the July dust period is marked by orange bars, the sampling day is indicated by a red arrow. Figure created by http://aeronet.gsfc.nasa.gov/cgi-bin/bamgomas_interactive on September 6th, 2016.

We changed the first paragraph of the section 2 Samples and methods to **"**Dust samples used in this study collected from the top of the tower building of the meteorological observatory of Izaña, Tenerife, Spain (28° 18' 33.8" N, 16° 29' 56.9" W, 2395 m a.s.l.). Details on the procedure and location can be found in Kandler et al. (2007). Particles were collected with a cascade impactor on carbon adhesive, with nominal stage size ranges of > 2.6 µm, 0.9–2.6 µm, and 0.1–0.9 µm (50 % efficiency cut-off aerodynamical particle diameter), of which the stages with > 0.9 µm were used for analysis. All samples were stored in a desiccator under dry conditions prior to analysis. The sample analyzed in the present work was collected during a 10 min period on 15 July 2005 at 09:33 h (UTC). It was selected as best-representing the campaign to achieve the greatest atmospheric relevance. Its composition is close to the mean campaign composition (cf. Kandler et al., 2007, Fig. 8), and the corresponding transport trajectory is central in the observed trajectory field (Fig. 1 and Kandler et al., 2007, Fig. 9). According to AERONET aerosol optical thickness data (Supplement Fig. 1), the concentration on the sampling day was also close to the average of the dust event lasting from July 12 to July 22, 2005.

Analysis was limited to particles with diameter < 5 μm, as too few larger ones were available**"**

SEM-EDXS results of two impact stages were added to Table 1.

Table 1. Mineral number % of Saharan dust based on SEM-EDXS analyses of single particles.

Size	No. of particle	Total clay minerals	ISCMs*	Ka	Ch	Bt	Q	P	Kf	Am	Ca	D	Fe	Ti	Gy	Sp	Ap
Saharan dust, Tenerife (This study)																	
0.9-2.5 μm	*n*=1191	1005	868	131	6	0	105	21	17	1	12	5	8	8	9	0	0
	%	84.4	72.9	11.0	0.5	0.0	8.8	1.8	1.4	0.1	1.0	0.4	0.7	0.7	0.8	0.0	0.0
> 2.5 μm	*n*=435	314	260	45	8	1	59	23	17	1	9	1	3	2	4	1	1
	%	72.7	60.2	10.4	1.9	0.2	13.7	5.3	3.9	0.2	2.1	0.2	0.7	0.5	0.9	0.2	0.2
Total	*n*=1626	1319	1128	176	14	1	164	44	34	2	21	6	11	10	13	1	1
	%	81.1	69.4	10.8	0.9	0.1	10.1	2.7	2.1	0.1	1.3	0.4	0.7	0.6	0.8	0.1	0.1
Asian dust, Korea (Jeong and Achterberg, 2014)**																	
%		56.1	48.4	1.8	3.9	2.1	18.7	10.5	4.0	0.7	6.5	1.0	1.2	0.2	0.8	0.2	0.2

*ISCM=illite-smectite series clay minerals, Ka=kaolinite, Ch=chlorite, Bt=biotite, Q=quartz, P=plagioclase, Kf=K-feldspar, Am=amphibole, Ca=calcite, D=dolomite, Fe=iron (hydr)oxide, Ti=Ti oxide, Gy=gypsum, Sp=sphene, Ap=apatite.

** Average value of the SEM-EDXS results from three Asian dust samples presented in Jeong and Achterberg (2014). Vaules are slightly differernt from those in Jeong and Achterberg (2014) by the change of mineral species considered for quantification.

Comment (2) Criteria used for the identification of predominant minerals both from EDX data and electron diffraction/lattice fringe imaging should be presented in supporting information.

Reply and Changes in the manuscript (2) The procedures of mineral identification using EDXS, lattice fringe imaging, and electron diffraction are now provided in **supplement information** as attached at the end of this letter.

Comment (3) In the section 3.1, the relative abundance of clay mineral particles obtained from SEM-EDXS data (Table 1) for the Tenerife sample is directly compared with the total clay content (in wt%?) determined by XRD for a Cape Verde sample, but they are two different physical parameters. This point should be clarified.

Reply (3) Both data are incomplete because of the lack of either XRD or SEM-EDXS data. This is caused by the nonavailability of samples suitable for XRD in Tenerife and SEM-EDXS single particle analysis in Cape Verde (sampling campaigns were done many years ago).

Changes in the manuscript (3) We deleted the comparison of Tenerife SEM-EDXS data to Cape Verde XRD data.

Comment (4) In the section 3.3, the volume of iron (hydr)oxides in the dust particles is estimated. Two dimensions of the iron grains in dust are obtained from the bright-field TEM images, but how is measured the third dimension, notably for internal grains? From EDX maps? It should be explained.

Reply (4) The third dimension of iron (hydr)oxides was not measured. The percentage was derived by measuring the relative area of the iron (hydr)oxides from TEM images by counting pixel using the lasso tool and histogram of ADOBE PHOTOSHOP. In fact, the FIB slices cannot be used to measure the volume of mineral grains included in the dust particles because large portion of the included grains were commonly removed by the FIB work. In addition, we do not have any method to directly measure the volume of included submicron to nano-sized grains yet. However, the area% of included grains approximates the volume% (Vepraskas and Wilson, 2008, Soil Micromorphology: concepts, techniques, and applications, in: Methods of Soil Analysis, Part 5). Although the third dimension of iron (hydr)oxides could not be measured from the FIB slices, the area% of iron (hydr)oxide grains in a dust particle approximates their volume %. If the iron (hydr)oxide grains imaged by TEM are the only iron (hydr)oxides included in the dust particle, the volume of host particle would be enormously larger than the volume of tiny iron (hydr)oxides in comparison to corresponding areas because volume is proportional to the cube of the diameter. However, the FIB slices expose a cross section of iron (hydr)oxide grain which was randomly selected from many iron (hydr)oxide grains dispersed through the dust particle. Thus, area% approximates volume%. We would like to keep volume%.

Changes in the manuscript (4) We inserted following sentences: "Although the third dimension could not be measured, the area% of iron (hydr)oxide grains approximates volume% because tiny iron (hydr)oxide grains had been randomly dispersed through the dust particle (Vepraskas and Wilson, 2008)."

Comment (5) The section "3.5 Shape of dust particles" notably presents the methodology to measure the total particle volume, so it should be inserted before the part 3.3 in which particle volumes are presented and also discussed (sup Table 1).

Reply (5) We are interested in the volume of iron (hydr)oxides. The area of iron (hydr)oxides was measured by counting pixel using the lasso tool and histogram of ADOBE PHOTOSHOP. We did not measure their *a*, *b*, and *c* dimensions.

Changes in the manuscript (5) We would like to keep part 3.5.

Technical correction (6) (Avila et al., 1997) is cited in the introduction, but (Avila et al., 1996) is listed in the bibliography.
Reply and Changes in the manuscript (6) The bibliography was corrected to 1997.

Technical correction (7) (Conny, 2013) is cited in the introduction, but it is not among the listed references.
Reply and Changes in the manuscript (7) Conny (2013) was added to the list.

Technical correction (8) Figure 1: What is the level high of the arrival air masses for the backward trajectory calculations by HYSPLIT? It should be mentioned in the Figure caption.
Reply and Changes in the manuscript (8) "Izana" was changed to Izana (2400 m asl.).

Technical correction (9) Figure 2: The meaning of yellow lines is given two times in the Figure caption.
Reply and Changes in the manuscript (9) One of the repeated sentences was deleted.

Supplement Information – Mineral identification

Minerals have their own crystal structures and chemical compositions. Thus, mineral identification using TEM is based on the lattice-fringe imaging and electron diffraction providing structural information and EDXS providing chemical information. Precise identification of all the minerals in the FIB slice to the species level is practically impossible because of beam damage, high vacuum, lower reliability of lattice fringes/electron diffraction data in comparison with XRD, and enormous time required.

TEM identification of nonphyllosilicate minerals

The identification of quartz, K-feldspar, plagioclase, calcite, amphibole, dolomite, titanite, apatite, and gypsum was straightforward based on their characteristic EDX spectra (Fig. S1). Although we could not identify mineral species of K-feldspar (sanidine, orthoclase, microcline), plagioclase (albite, oligoclase, andesine...), and amphibole (tremolite, actinolite, hornblende...) using time-consuming complex operation, the purpose of current mineral dust research was satisfied by grouping similar mineral species. Silica phase of the mineral dust from desert was almost quartz, consistent with XRD although few amorphous silica was identified by electron diffraction.

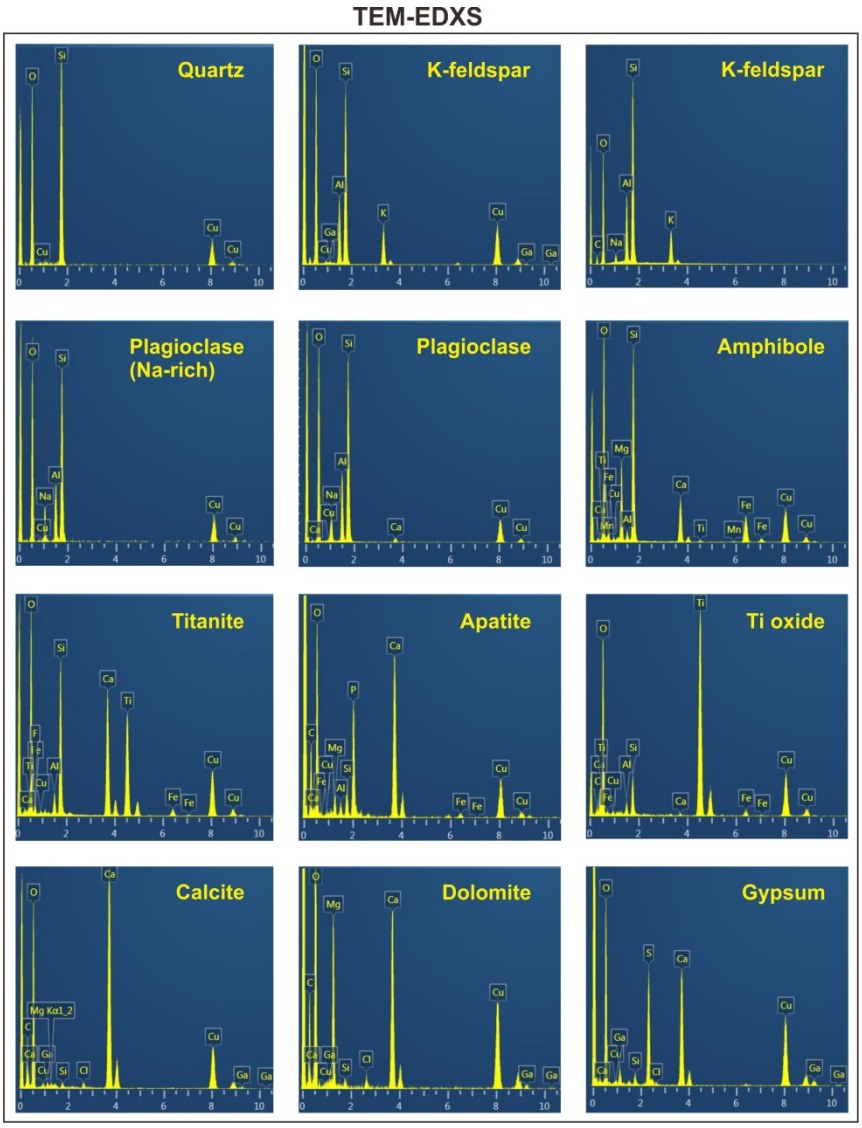

Fig. S1. TEM EDXS patterns of constituent minerals of dust particles obtained from the cross-sectional slices prepared by FIB.

TEM identification of phyllosilicate minerals

Phyllosilicate minerals were abundant in the mineral dust. The identification of muscovite, biotite, and chlorite was rather straightforward from their characteristic chemical compositions with the aid of lattice-fringe imaging (Fig. S2). However, the identification of nano-thin phyllosilicates (clay minerals) was difficult because of their breakdown under electron beam and small grain size below the minimum diameter of electron beam for EDXS. They occurred often as agglomerates. In addition, mixed layering of illite and smectite is common in natural soils. The identification of clay minerals was based on lattice fringes and chemical compositions: 1.0 nm for illite, ~1.0 nm for smectite and vermiculite, and ~7.0 nm for kaolinite (Fig. S2). Kaolinite was directly identified from its EDXS with the aid of lattice fringe imaging. However, illite, smectite, and illite-smectite mixed layers could not be separately identified each other because smectite was contracted under the high vacuum of the TEM chamber, showing ~1.0 nm lattice fringes similar to those of illite. Although EDXS can be used for identifying illite and smectite with interlayer cations K and Ca, respectively, they cannot be separately analyzed using EDXS, even when using an electron beam as small as possible. Therefore, we could not distinguish between nano-thin illite, smectite, and their mixed-layers, using conventional TEM work. To avoid over-interpretation, nano-thin platelets of clay minerals showing ~1.0 nm lattice fringes with varying K and Ca contents were grouped into illite-smectite series clay minerals (ISCMs). ISCMs are nano-scale mixtures of nano-thin platelets of illite, smectite, and illite-smectite mixed-layers.

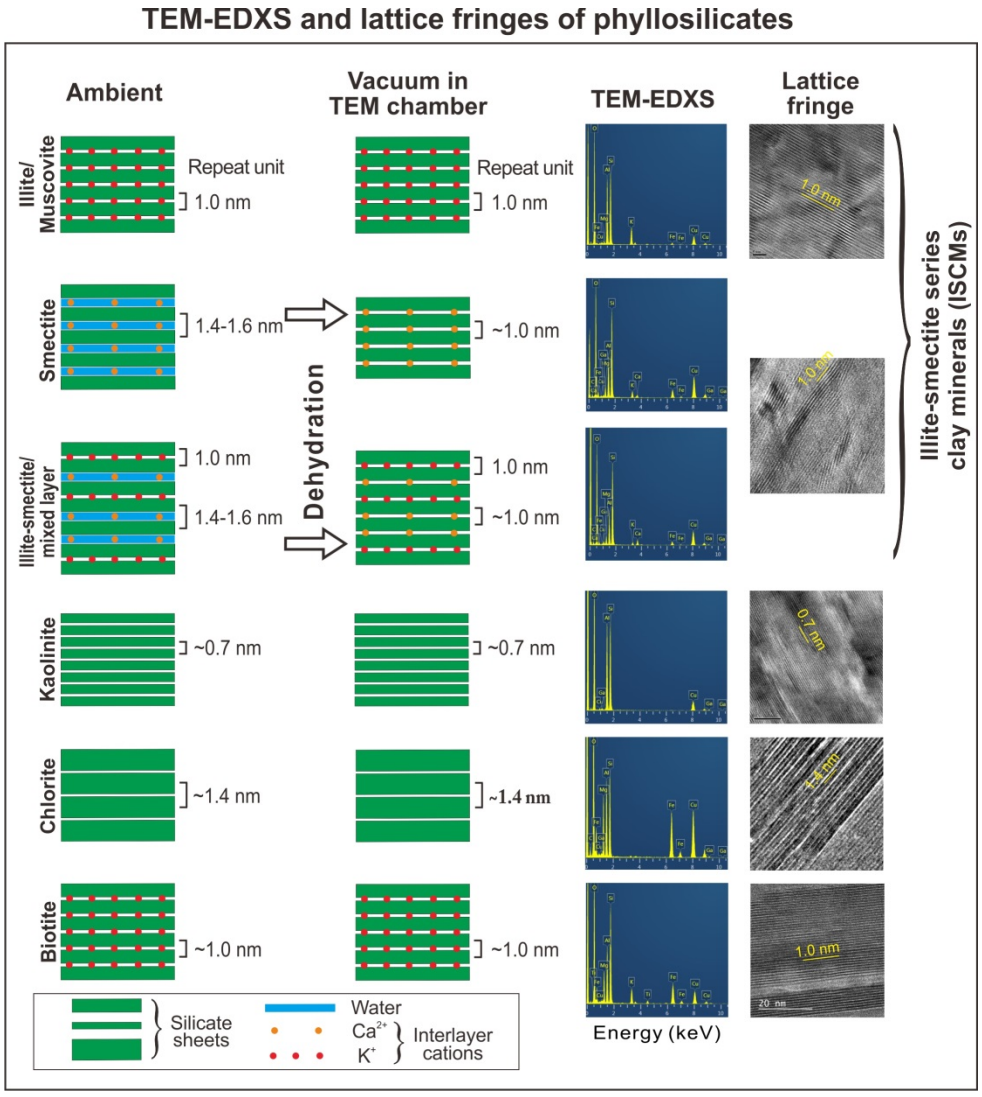

Fig. S2. Identification of phyllosilicates using TEM-EDXS and lattice fringes.

TEM identification of iron (hydr)oxides

Mineralogical identification of iron (hydr)oxides was also challenging. EDXS could not be used for the identification. Electron diffraction and lattice-fringe imaging should be used in combination as shown in Fig. S3. However, many iron (hydr)oxide grains could not be identified because of the overlap of many *d*-spacings, varying crystallographic orientation, and tiny grain sizes. Thus, we used species names only in cases in which mineral species were identified unambiguously by lattice fringe imaging and electron diffraction; in other cases, we used the collective term "iron (hydr)oxide".

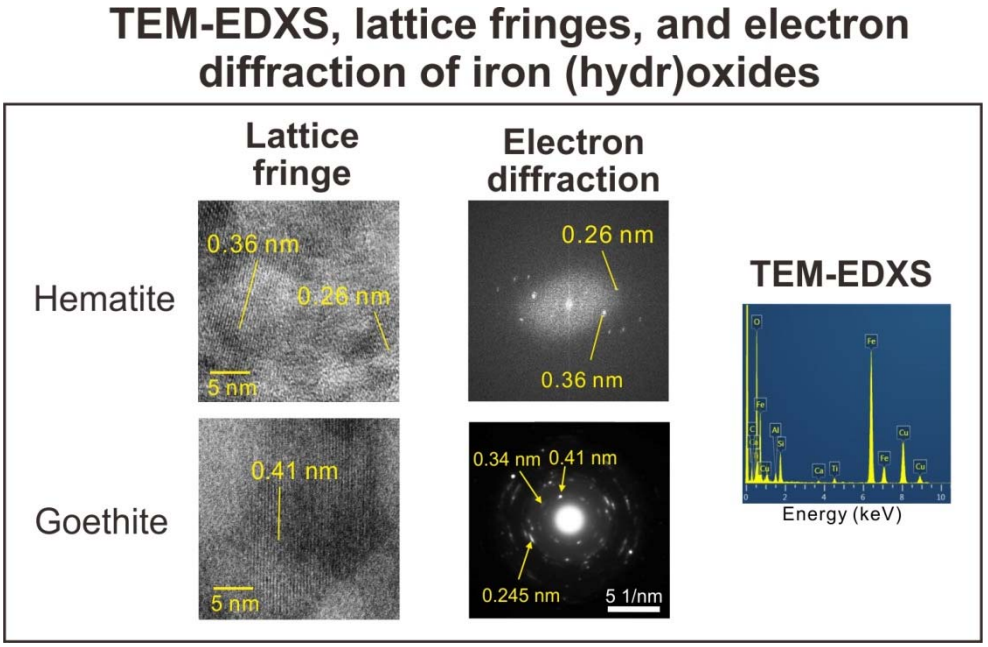

Fig. S3. Identification of phyllosilicates using lattice fringes and electron diffraction.

Mineralogical classification of dust particles using SEM-EDXS

Dust particles are essentially mixtures of mineral grains of diverse species and sizes. In case the quantity of powder dust samples is sufficient (~several hundred mg), XRD method is best for the determination of mineral composition. SEM-EDXS analyses of individual particle can be used when powder samples are insufficient or non-available. Ideally, mineral composition of individual dust particle can be determined by mixing several minerals to get the overall chemical composition of the particle. Then, the summation of the mineral compositions of thousands of dust particles considering their volume would lead to the mineral composition of bulk dust. However, the irregular morphology of dust particles prohibits the accurate determination of dust particles due to the difficulty of calibration. In addition, the chemical compositions of constituent minerals are varied. Prior to the development of reliable quantitative analysis procedure based on SEM for the mineral composition of individual dust particle, we adopted semi-quantitative approach. Since dust particles are generally dominated by one mineral species or group, we have determined the predominant mineral of a dust particle referring to the EDXS patterns of pure minerals as shown in Figs. S1 and S2. In case particles show intermediate EDXS pattern (Fig. S4), half of the particle was counted (0.5). Summation of the counts led to the approximate mineral composition of bulk dust. Although the procedure is evidently semi-quantitative, SEM-EDXS results were consistent with XRD results in the recent analyses of Asian dust (Table 1 in Park and Jeong (2016), Journal of the Mineralogical Society of Korea, 29, 79–87).

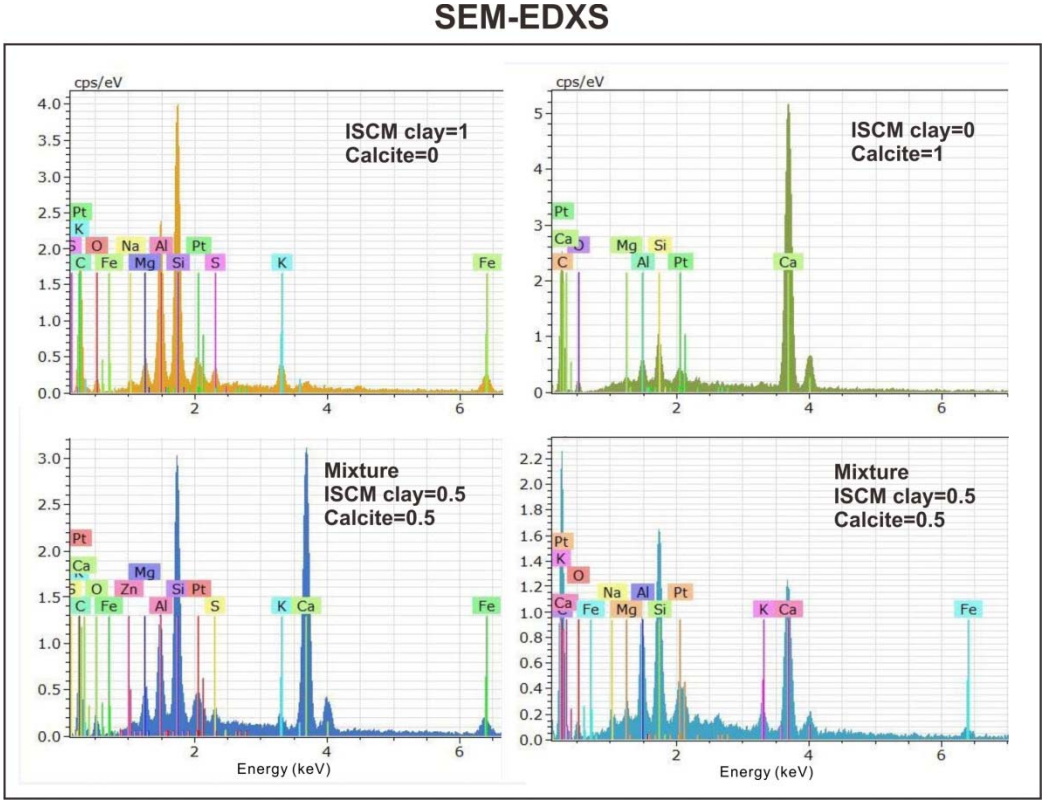

Fig. S4. SEM-EDXS of dust particles.

Park and Jeong (2016)

Table 1. Mineral compositions of Asian dusts determined by XRD analysis and SEM-EDS single particle analysis

Minerals	Asian dust XRD				
	Feb 22 2015	Mar 18 2014	Mar 31 2012	Mar 20 2010	Average
	(This study)	(Jeong and Achterberg, 2014)			
ISCMs	55	60	42	50	51
Kaolinite	2	1	3	4	3
Chlorite	5	3	6	7	5
Total clay	*62*	*64*	*52*	*61*	59
Quartz	18	14	23	15	17
Plagioclase	10	11	15	10	12
K-feldspar	4	0	6	2	3
Amphibole	0	0	1	2	1
Calcite	5	5	2	5	4
Gypsum	1	6	2	6	4
Total	100	100	100	100	100
	SEM single particle analysis				
ISCMs	57	54	48	54	52
Kaolinite	2	1	3	2	2
Chlorite	3	2	4	6	4
Total clay	*62*	*58*	*55*	*62*	58
Quartz	19	19	21	17	19
Plagioclase	9	11	11	10	11
K-feldspar	3	4	5	3	4
Amphibole	0	1	1	0	1
Calcite	4	7	7	6	7
Gypsum	2	0	1	1	1
Total	100	100	100	100	100

We will prepare final version considering comment and reply above.

Sincerely

On behalf of co-authors

Gi Young Jeong
Corresponding Author

Mineralogical properties and internal structures of individual fine particles of Saharan dust

Gi Young Jeong[*,1], Mi Yeon Park[1], Konrad Kandler[2], Timo Nousiainen[3], Osku Kemppinen[3,4]

[1]Department of Earth and Environmental Sciences, Andong National University, Andong 36729, Republic of Korea
[2]Institut für Angewandte Geowissenschaften, Technische Universität Darmstadt, Schnittspahnstr. 9, 64287 Darmstadt, Germany
[3]Earth Observation, Finnish Meteorological Institute, P.O. Box 503, FI-00101, Helsinki, Finland
[4]Department of Physics, Kansas State University, 116 Cardwell Hall, Manhattan, KS 66506, USA

[*]*Correspondence to*: G.Y. Jeong (jearth@anu.ac.kr)

Abstract: Mineral dust interacts with incoming/outgoing radiation, gases, other aerosols, and clouds. The assessment of its optical and chemical impacts requires knowledge of the physical and chemical properties of bulk dust and single particles. Despite the existence of a large body of data from field measurements and laboratory analyses, the internal properties of single dust particles have not been defined precisely. Here, we report on the mineralogical organization and internal structures of individual fine (< 5 μm) Saharan dust particles sampled at Tenerife, Canary Islands. The bulk of Tenerife dust was composed of clay minerals (81%), followed by quartz (10%), plagioclase (3%), and K-feldspar (2%). Cross-sectional slices of Saharan dust particles prepared by the focused ion beam technique were analyzed by transmission electron microscopy (TEM) to probe the particle interiors. TEM analysis showed that the most common particle type was clay-rich agglomerate, dominated by illite–smectite series clay minerals with subordinate kaolinite. Submicron grains of iron (hydr)oxides (goethite and hematite) were commonly dispersed through the clay-rich particles. The median total volume of the iron (hydr)oxide grains included in the dust particles was estimated to be about 1.5 vol%. The average iron content of clay minerals, assuming 14 wt% H_2O, was determined to be 5.0 wt%. Coarse mineral cores, several micrometers in size, were coated with thin layers of clay-rich agglomerate. Overall, the dust particles were roughly ellipsoidal, with an average axial ratio of 1.4:1.0:0.5. The mineralogical and structural properties of single Saharan dust particles provide a basis for the modeling of dust radiative properties. Major iron-bearing ~~constituent~~ minerals, such as illite–smectite series clay minerals and iron (hydr)oxides, were commonly submicron- to nano-sized, possibly enhancing their biogeochemical availability to remote marine ecosystems lacking micronutrients.

1 Introduction

Mineral dust affects Earth's climate and ecosystems via interaction with electromagnetic radiation (Sokolik and Toon, 1996; Tegen and Lacis, 1996; Formenti et al., 2011), acidic gases, and anthropogenic aerosols (Dentener et al., 1996; Ooki and Uematsu, 2005; Laskin et al., 2005), by becoming ice ~~condensation~~ nuclei (Kulkarni and

Dobbie, 2010; Freedman, 2015), and delivering micronutrients to remote ocean and terrestrial environments (Swap et al., 1992; Mahowald et al., 2009; Johnson and Meskhidze, 2013). To understand the interactions of dust with environments, a wide range of studies have been carried out to characterize the physical and chemical properties of bulk dust and individual dust particles, such as the size distribution (Seinfeld et al., 2004), particle morphology (Okada et al., 2001; Reid et al., 2003), chemical composition (Coude-Gaussen, 1987; Okada et al., 1990; Kanayama et al., 2002; Ro et al., 2005; Klaver et al., 2011; Arimoto et al., 2004), and mineral composition (Glaccum and Prospero, 1980; Avila et al., 1997; Shi et al., 2005; Kandler et al., 2007, 2009; Jeong, 2008; Shao et al., 2008; Jeong et al., 2014).

Of these properties, the internal structure and mineralogical properties of individual dust particles have been the least studied, largely due to the lack of suitable and reliable methods. Scanning electron microscopy (SEM) combined with energy-dispersive X-ray spectrometry (EDXS) has been applied to obtain information on the two-dimensional (2D) morphology and overall chemical composition of individual particles (Okada et al., 1990; Anderson et al., 1996; Ro et al., 2005; Gao et al., 2007). These individual dust particles, however, are usually composed of polymineralic/polycrystalline mixtures of diverse minerals (Falkovich et al., 2001; Jeong, 2008), and SEM-EDXS cannot easily yield information on their internal structures and mineralogical properties. Focused ion beam (FIB) technique was applied to expose the cross sections of urban dust particles for SEM analysis (Conny, 2013). A practical method for the acquisition of data on the internal properties, however, was transmission electron microscopy (TEM) for thin cross-sectional slices prepared from single dust particles by FIB technique. With these improvements, Jeong and Nousiainen (2014) reported internal structures and mineralogical makeup of single particles of Asian dust which could be classified into several structural types.

Knowledge of the internal properties of dust particles is essential for the establishment of a realistic model of mineral dust, which would enable assessment of its radiative properties and biogeochemical contributions. Based on the findings byof Jeong and Nousiainen (2014), Kemppinen et al. (2015) calculated the optical properties of internally inhomogeneous single dust particles, and showed that their light scattering properties depended significantly on their internal structures and iron oxide mineralogy of dust particles, as well as how they were accounted for in the modeling. The difficulty of accurately mimicking the impacts of these inhomogeneities on scattering by effective medium approximations suggests that accurate optical models of dust particles should account explicitly for at least the most impactful types of internal inhomogeneity. Regarding biogeochemical contributions, mineral dust transported to remote marine ecosystems is reportedly responsible for phytoplankton blooms due to the supply of iron, and terrestrial ecosystems are also considerably impacted (Swap et al., 1992; Boyd et al., 2000; Jickells et al., 2005; Formenti et al., 2011). The bioavailability of iron in oceans depends largely on its mineralogical form in the dust particles (Cwiertny et al., 2008; Journet et al., 2008), which can also be investigated on FIB slices using TEM.

The Saharan desert is the largest single source of atmospheric dust. Large volumes of this emitted dust are transported over long distances across the Atlantic Ocean and Mediterranean Sea. Although the physical, chemical, and mineralogical properties of bulk Saharan dust and single particles have been investigated (Falkovich et al., 2001; Reid et al., 2003; Kandler et al., 2007, 2009; Formenti et al., 2011), the mineralogical

compositions and ~~internal~~ structures of ~~single~~ dust particle interiors have not been studied. Jeong and Achterberg (2014) attempted TEM analysis of FIB slices prepared from individual Saharan dust particles, but unsuccessfully as original individual dust particles could not be identified on their filter heavily deposited with dust. To extend the mineralogical and structural analyses of Asian dust particles conducted by Jeong and Nousiainen (2014), we have now conducted a similar analysis of FIB slices prepared from fine Saharan dust particles collected specifically for single-particle electron microscopic analysis.

2 Samples and methods

Dust samples used in this study collected from the top of the tower building of the meteorological observatory of Izaña, Tenerife, Spain (28° 18' 33.8" N, 16° 29' 56.9" W, 2395 m a.s.l.). Details on the procedure and location can be found in Kandler et al. (2007). Particles were collected with a cascade impactor on carbon adhesive, with nominal stage size ranges of > 2.6 µm, 0.9–2.6 µm, and 0.1–0.9 µm (50 % efficiency cut-off aerodynamical particle diameter), of which the stages with > 0.9 µm were used for analysis. All samples were stored in a desiccator under dry conditions prior to analysis. The sample analyzed in the present work was collected during a 10 min period on 15 July 2005 at 09:33 h (UTC). It was selected as best-representing the campaign to achieve the greatest atmospheric relevance. Its composition is close to the mean campaign composition (cf. Kandler et al., 2007, Fig. 8), and the corresponding transport trajectory is central in the observed trajectory field (Fig. 1 and Kandler et al., 2007, Fig. 9). According to AERONET aerosol optical thickness data (Supplement Fig. 1), the concentration on the sampling day was also close to the average of the dust event lasting from July 12 to July 22, 2005. Analysis was limited to particles with diameter < 5 µm, as too few larger ones were available.~~Dust samples were collected from the top of the tower building of the meteorological observatory of Izaña, Tenerife, Spain (28° 18' 33.8" N, 16° 29' 56.9" W, 2395 m a.s.l.). Details on the procedure and location can be found in Kandler et al. (2007). Fine (< 5 µm) particles were collected with a cascade impactor on carbon adhesive for 10 min on 15 July 2005 at 09:33 h (UTC). All samples were stored in a desiccator under dry conditions prior to analysis.~~

Backward trajectories of air mass were calculated by HYSPLIT4 rev. 2015-06-16 (Stein et al., 2015). Fig. 1 shows the trajectory plots for the impactor sample. The atmospheric circulation on the sampling day was stable, with a continuous flow leaving the western Saharan desert at altitudes of 3–4 km and travelling over the ocean during the final 2 days before arrival under very dry conditions (10–30% relative humidity). Dust injection is assumed for parts of the trajectory, which were inside the modeled mixing layer. Northeastern Mauritania and southern Algeria are the most probable source regions for the analyzed sample. According to the trajectory analysis, the injected dust had travelled for a minimum of 4 days before it was collected at Izaña. Due to the dry conditions, however, considerable alteration of the dust components was not expected.

Dust particles were analyzed using a TESCAN LYRA3 XMH field emission scanning electron microscope equipped with a Bruker EDXS system. SEM images showed that the individual particles were sufficiently separated from each other, with no coagulation occurring during deposition. All the particles collected on the

impact stages were not analyzed. We selected rectangular areas of homogeneous particle distribution at low magnification, and then, EDXS patterns were obtained from all the particles in the areas. Total number of the analyzed dust particles was 1626: 1191 particles from the impact stage 0.9–2.6 μm, and 435 particles from the stage > 2.6 μm. EDXS patterns ~~of 1626 particles~~ were ~~obtained and~~ classified according to predominant mineral to obtain approximate mineral compositions of bulk dust (Supplement Information; Jeong, 2008; Jeong et al., 2014). The mineral composition obtained by this method is evidently semi-quantitative, considering large inherent uncertainty. Previous analyses of Asian dust, however, showed that SEM-EDXS results were consistent with XRD results (Park and Jeong, 2016). The 48 target particles for FIB work were selected according to the mineralogical types of the dust particles, reflecting~~considering~~ mineral ~~their~~ abundance of bulk dust determined by EDXS analyses: 21 particles from the impact stage 0.9–2.6 μm and 27 particles from the impact stage > 2.6 μm, respectively. Thus, the 48 FIB slices analyzed are representative of the Saharan dust particles collected on the sampler. However, three iron-enriched particles were selected for the identification of iron (hydr)oxide mineral species, which were not common.

Dust particles on the carbon adhesive were placed in a JEOL JIB-4601F FIB instrument to prepare thin cross-sectional slices (ca. 6 × 6 μm, <100 nm thickness). Detailed procedures of slice preparation using FIB techniques and a discussion of possible artifacts were provided in Jeong and Nousiainen (2014). The slices are cross sections along the shorter axes of the particles observed by SEM. A total of 48 FIB slices were prepared from 48 dust particles and analyzed using a JEOL JEM 3010 transmission electron microscope for lattice-fringe imaging and a JEOL JEM 2010 transmission electron microscope equipped with an Oxford X-MAX EDXS system for internal-structure imaging and chemical analysis. TEM images of 18 slices are presented here, and those of 30 slices are presented in Supplement~~ary~~ Fig. 2~~1~~.

Minerals in the FIB slices were identified by the combined use of EDXS, electron diffraction, and lattice fringe imaging. The identification criteria for ~~clay~~ minerals are summarized in Supplement Information~~Jeong and Nousiainen (2014)~~. Nano-thin platelets of illite–smectite series clay minerals (ISCMs) have been found commonly in TEM analyses of natural mineral dusts (Jeong et al., 2014; Jeong and Nousiainen, 2014; Jeong and Achterberg, 2014). They are nano-scale mixtures of nano-thin platelets of illite, smectite, and illite–smectite mixed layer clay minerals, all of which have lattice fringes measuring ~1.0 nm due to the dehydration of smectite interlayer water. Despite the differences in their chemical compositions, the routine identification of these minerals using TEM-EDXS is challenging because the electron beam diameter could not be reduced below ~100 nm without severe beam damage and count loss. Thus, to avoid over-interpretation of TEM data, nano-thin platelets of clay minerals showing ~1-nm lattice fringes with varying contents of interlayer K and Ca were grouped as ISCMs (Jeong and Nousiainen, 2014). In some cases, when the separate chemical identification of illite and smectite platelets was possible due to the large grain size, we used the terms illite and smectite.

The mineralogical identification of iron (hydr)oxide polymorphs was performed using electron diffraction and lattice fringe imaging. The routine unambiguous identification of all iron (hydr)oxide grains, however, was challenging due to the superimposition of d-spacings, varying crystallographic orientations, and often vague electron diffraction patterns. Thus, we used mineralogical names only in cases in which mineral species were

identified unambiguously by lattice fringe and electron diffraction; in other cases, we used the collective term "iron (hydr)oxide". Chemical compositions of ISCMs, illite, smectite, chlorite, and biotite were quantified by measuring X-ray intensities of Si, Al, Fe, Mg, Ti, K, Na, and Ca. The X-ray counts of the elements were converted to weight% using *k* factors determined experimentally from FIB slices of biotite and plagioclase of known composition from the Palgongsan granite (Jeong, 2000). More details can be found in Jeong and Achterberg (2014), except that this study used a more sensitive Oxford X-MAX EDXS detector ~~was used in this study~~. In this study, the term "particle" refers to an individual airborne solid object and the term "grain" refers to a particle constituent. In most cases, particles were agglomerates of grains.

3 Results and Discussion

3.1 Mineral composition of bulk dust

~~Analyses of S~~~~s~~ingle-particle SEM-EDXS data showed that dust particles in both size fractions were dominated by clay minerals including ISCMs and kaolinite. Dust particles of 0.9–2.6 µm in size, however, were slightly enriched in clay minerals in comparison with those of > 2.6 µm in size, while non-clay minerals including quartz, plagioclase, and K-feldspar were rather enriched in coarser particles (> 2.6 µm). Average mineral composition was ISCMs ~~were the dominant mineral group (~~69%~~)~~, ~~followed by~~ kaolinite ~~(~~11%~~)~~, quartz ~~(~~10%~~)~~, plagioclase ~~(~~3%~~)~~, K-feldspar ~~(~~2%~~)~~, calcite ~~(~~1%~~)~~, chlorite ~~(~~1%~~)~~, iron (hydr)oxide ~~(~~1%~~)~~, titanium oxide ~~(~~1%~~)~~, and gypsum ~~(~~1%~~)~~ (Table 1). The total clay mineral content was 81%. ~~Although we could not obtain X-ray diffraction (XRD) data for bulk Tenerife dust, these single-particle SEM-EDXS data were well matched with XRD data obtained for Saharan dust sampled in Cape Verde (Table 2 in Jeong and Achterberg, 2014). We assume that the Cape Verde sample has similar source regions, as transport of dust from Mauritania, Mali, and Algeria to Cape Verde in winter is very common (Chiapello et al., 1997; Knippertz et al., 2011). The total clay content determined by XRD for the Cape Verde dust sample was 81%, matching the proportion obtained using single-particle SEM-EDXS data in this study.~~ Scheuvens et al. (2013) have proposed, among others, a Ca/Fe ratio for source discrimination of Saharan dust, with very low Ca/Fe ratios for the probable regions. The very low calcite content of the Tenerife Saharan dust sample is thus in agreement with the identification of source regions by backward trajectory analysis.

3.2 Internal structures of individual dust particles

3.2.1 Clay-rich particles

Clay-rich particles were the most common (Fig. 2). They were dominated by ISCMs, which were loose, sub-parallel agglomerates of slightly curved nano-thin platelets with 1.0-nm lattice fringes (Fig. 2a). The

morphological features of ISCMs contrasted with those of illite which were thick, straight, and compact (Fig. 2a). Very few clay-rich particles were pure ISCMs (Fig. 2b) or kaolinite (Fig. 2c). They were commonly mixtures with dominant ISCMs and subordinate kaolinite.

3.2.2 Large minerals with clay-rich coatings

Large mineral grains, such as quartz, plagioclase, and K-feldspar, were usually coated with thin clay layers composed of ISCMs and kaolinite. The large core grains were roughly equidimensional, with irregular surfaces (Fig. 3). The thicknesses of the clay coatings varied due to the irregular surface topographies of the substrates. Our observations confirmed a near absence of clean surfaces free of clay coatings on quartz, plagioclase, and K-feldspar. Large phyllosilicate grains, such as illite, biotite, and chlorite, were plates with smooth surfaces coated with clays (Fig. 4). Submicron grains of iron oxides were found at the interfaces between clay coatings and substrates (Fig. 3a, b) or scattered through the clay coatings (Fig. 4c).

3.2.3 Intergrade particles

Some dust particles were intergrades between clay-rich particles and clay-coated minerals. The intergrade particles were composed of abundant clays with large mineral inclusions of K-feldspar (Fig. 5a), dolomite (Fig. 5b), and calcite (Fig. 5c), as well as quartz, plagioclase, and large phyllosilicates such as biotite, chlorite, and illite (Supplement~~ary~~ Fig. 2~~1~~). Clays consisted mostly of ISCMs and kaolinite with submicron grains of iron (hydr)oxides. The clay matrices of the intergrade particles shown in Fig. 5b and c included palygorskite fibers.

3.3 Iron (hydr)oxides

Dust particles dominated by iron (hydr)oxides were rare (Fig. 6). Most iron (hydr)oxides occurred as submicron grains dispersed in the clay matrices of clay-rich particles (Fig. 7). Although the absolute content of iron (hydr)oxides in mineral dust is small (Lafon et al., 2006; Jeong, 2008; Jeong et al., 2014; Journet et al., 2014), the role of these components in light scattering deserves attention due to their high refractive index/absorption (Sokolik and Toon, 1999; Lafon et al., 2006; Kemppinen et al., 2015). The species, volume%, grain size, and distribution of iron (hydr)oxides in the interiors of dust particles therefore must be considered in the modeling of optical properties.

The mineral species of iron (hydr)oxides identified by electron diffraction and lattice fringes were goethite (Fig. 7a, c, d) and hematite (Fig. 7a, b, e). We could not estimate the relative proportions of goethite and hematite quantitatively because the identification of iron (hydr)oxides was not a routine procedure. Qualitatively, however, goethite grains were likely more common than hematite, similar to the findings of Lafon et al. (2006). Iron (hydr)oxides were included in 40 of the 48 FIB slices. Goethite was positively identified by electron diffraction and lattice imaging in 19 slices, hematite was identified in eight slices, and magnetite was identified in two slices.

We estimated the total volume of iron (hydr)oxides in the dust particles from their areas measured in bright-field TEM images using the lasso tool and histogram of ADOBE PHOTOSHOP CS5, as these minerals occur as dark grains due to their high atomic numbers. However, we could not perform grain-by-grain identification or measurement of the numerous iron (hydr)oxide grains, as discussed in section 2. Although the third dimension could not be measured, the area% of iron (hydr)oxide grains approximates volume% because tiny iron (hydr)oxide grains had been homogeneously distributed through the dust particle (Vepraskas and Wilson, 2008). The abundance of iron (hydr)oxide grains ranged widely, from high (e.g., 50% in Fig. 7a, 28% Fig. 7e) to moderate (e.g., 15% Fig. 7b, 9% Fig. 7c), sparse (e.g., 3% Figs. 2c and 7d, 0.7% Fig. 3c), and absent (e.g., Figs. 2a and b). The median volume of iron (hydr)oxides in 48 dust particles was 1.5%. Half of the values fell between 1% and 10% (Supplement~~ary~~ Table 1). Some of the dark grains in the TEM images were titanium oxides (Fig. 2b), although their contents were lower than those of iron (hydr)oxides in most particles. Thus, the measured volume% of iron (hydr)oxides must be considered a maximum value, as we could not account for the titanium oxides explicitly.

Grain sizes of iron (hydr)oxides ranged from a few hundred to several tens of nanometers. All longer axes of iron (hydr)oxide grains in the interiors of dust particles fell within the submicron range; most were <0.5 μm with common small grains of several tens of nanometers long (Fig. 7). The grains were well dispersed throughout the clay-rich medium, in contrast to the findings of Deboudt et al. (2012), who detected them more commonly on the surface.

3.4 Chemical composition of clay minerals

.

The chemical compositions of clay minerals from the Tenerife dust particles, determined by TEM-EDXS of FIB slices, were plotted on a K–Fe diagram (Fig. 8). The data distribution was consistent with that for Saharan dust collected in Cape Verde (Fig. 6 in Jeong and Achterberg, 2014). Almost all data plotted between ISCMs and kaolinite, confirming the higher kaolinite content of Saharan dust. The average elemental composition of clay minerals, based on 343 EDXS analyses and assuming 14 wt% H_2O, was Si 22.4, Al 13.2, Fe 5.0, Mg 1.8, Ti 0.2, K 1.2, Na 0.5, and Ca 0.4 wt%. The average iron content (5.0%) of the clay minerals in the Tenerife dust is consistent with that of the clay minerals in Cape Verde dust. The chemical compositions of ISCMs are plotted in the boxed region of Fig. 8, as derived in Jeong and Achterberg (2014). The average chemical formula of the Saharan dust ISCMs was $K_{0.17}Na_{0.09}Ca_{0.03}(Al_{1.43}Fe^{3+}_{0.38}Mg_{0.36}Ti_{0.01})(Al_{0.50}Si_{3.50})O_{10}(OH)_2$.

3.5 Shape of dust particles

The 2D shapes of dust particles have been approximated by ellipses with varying aspect ratios (e.g., Reid et al., 2003). Although the three-dimensional (3D) shapes of the particles resemble ellipsoids, they are – due to the lack of information on the third dimension – usually assumed to be spheroids in particle size analyses (Reid et al., 2003; Kandler et al., 2009; Jeong et al., 2014) and in optical modeling (Mishchenko et al. 1997; Nousiainen and

Vermeulen 2003; Dubovik et al., 2006, Merikallio et al., 2011). As a byproduct of FIB work on studies of dust interiors, the thicknesses of the particles can be derived from TEM images of the cross sections (Fig. 9). The two longer axes (*b* and *c*) of the ellipsoids were measured from SEM images, and the short axis (*a*) was measured from TEM cross-section images. The average axial ratios of 48 particles, obtained by dividing the lengths of axes *a* and *c* by that of axis *b*, were 1.4±0.3 (*c*/*b*) and 0.5±0.3 (*a*/*b*), respectively (Supplementary Table 1). The axial ratios of ellipsoids varied slightly, depending on the major mineral components of the particles. The *a*/*b* ratios were highly dependent on the mineralogical types of the particles; the average of this ratio was 0.5 in clay-rich particles; 0.7 in quartz, plagioclase, and K-feldspar with clay coatings; and 0.2 in particles consisting of coarse platy phyllosilicate minerals with clay coatings (Supplementary Table 1). The average of c/*b* ratio was 1.3 in clay-rich particles, and ~1.5 in coarse minerals with coatings.

3.6 Comparison with single-particle properties of Asian dust

The clay content of Saharan dust (81%) is higher than that of Asian dust (57%) (Table 1). Previous data showed that total clay content of Saharan dust ranged from 61% to 73% in the samples of the Atlantic islands (Glaccum and Prospero,1980), from 56% to 81% in the dustfall collected in Spain (Avila et al., 1997), and around 81% in two Saharan dust samples collected in Cape Verde (Jeong and Achterberg, 2014). Total clay content of Asian dust ranged from 28% to 50% in Beijing, China (Shao et al., 2008) and around 57% in Korea (Jeong and Achterberg, 2014). Thus, clay minerals are likely enriched in Saharan dust in comparison with Asian dust. Mineral compositions of clays also differ slightly between dusts. The analyzed Saharan dust sample is distinct from Asian dust due to its higher kaolinite content and lower chlorite content. The average Fe wt% of the clay minerals in Asian dust was 6.7%, which was slightly higher than that for Saharan dust (5%). The lower iron content of Saharan dust clay minerals is consistent with the lower chlorite content and the higher kaolinite content. ISCMs are the major mineral components of both Saharan and Asian dusts. Assuming K fixation in the illite interlayer (Jeong et al., 2004), the proportion of the illitic component of ISCMs was lower in the Tenerife Saharan dust (K = 1.51% on average) than in Asian dust (K = 2.2%).

The internal structures of the Saharan dust particles are basically similar to those of Asian dust particles, which were grouped into three types: type I, large non-clay grains with clay coatings; type II, clay-rich agglomerates with inclusions of non-clay mineral grains; and type III, large platy minerals with clay coatings. The dust particles shown in Figs. 2, 5, and 7 have Type II internal structures. Those shown in Figs. 3 and 4 have type I and type III internal structures, respectively. Irregular pores of varying sizes were reported in the interiors of Asian dust particles (Jeong and Nousiainen, 2014). Recent modeling of the optical properties of mineral dust showed that the internal pores of dust particles affect these properties (Kemppinen et al., 2015). Pores in the interiors of Tenerife Saharan dust particles, however, were rather scarce and small (Figs. 2b, 3c, and 5c; Supplementary Fig. 2~~1~~). The fine sizes of particles analyzed in this study may explain these findings. No particle observed by SEM exceeded 10 μm (most were < 5 μm), as large particles were rare in the probed dust event. We cannot exclude the possibility that coarse particles have larger pores due to increased heterogeneity from the

mixing of different mineral species, grain sizes, and surface properties. TEM analyses of additional dust samples, particularly those containing coarser particles, are required.

3.7 Implications for dust optical properties and micronutrient transport

In most applications, the dust particle optical properties are still based on the assumption of particle homogeneity (Nousiainen and Kandler, 2015; Kahnert et al., 2016). Based on the analysis of particle interiors of Asian dust by Jeong and Nousiainen (2014), Kemppinen et al. (2015) assessed the impacts of various types of observed inhomogeneity on the dust particles' optical properties. Their conclusion was clear: dust particles exhibit many types of inhomogeneity whose impacts on the optical properties cannot be accurately mimicked by homogeneous particle models. The impact of iron oxides in particular, whether present in isolated grains or mixed within the clay coating, could not be properly accounted for by any tested means of making the whole particles homogeneous. In addition, the presence of internal cavities led to impacts on optical properties that were challenging to mimic with homogenized particles.

The problem with iron oxides is that, at solar short-wave frequencies, their complex refractive indices differ substantially from those minerals that make most of the particle volume: the real part of refractive index can be easily a factor of two larger for the iron oxide, and the imaginary part tend to be larger by many orders of magnitude. A high imaginary part means that the particle interior is strongly absorbing, but the high real part may make it difficult for the radiation to penetrate through the particle surface to be absorbed. However, when a mixing formula is applied to average the refractive indices of the component materials, the typically small amounts of iron oxides are not sufficient to increase the real part of the refractive index much above that of the dominating minerals; whereas, the extremely large difference in the imaginary parts makes the whole particle interior much more absorptive. As a result, the homogenized particle will absorb light much more efficiently than either an external mixture or a model where the iron oxide grain would be present as an inclusion in a dust particle. The mixing of constituent minerals into a single, effective refractive index for model dust particles will thus lead to too much absorption and too low a single-scattering albedo.

Saharan dust was found to exhibit many types of inhomogeneity present also in Asian dust. Therefore, it appears plausible that the using homogeneous particle models for Saharan dust would result in similar potential errors as was reported by Kemppinen et al. (2015) for the Asian dust. There are, however, some differences to note. First, Saharan dust appeared to have fewer and smaller internal pores. Second, their iron oxide content was somewhat smaller. Both of these effects alone suggest a smaller impact on the optical properties due to the inhomogeneity. However, it does not mean that the impacts could be ignored, and it is further possible that the simultaneous decrease in pores and iron oxides changes the impacts. Therefore, explicit simulations to quantify the impacts are in order, and planned for in the future.

Saharan dust is a carrier of inorganic nutrients to remote ecosystems. Iron is an element limiting phytoplankton growth in remote ocean ecosystems. The modeling of iron supply to global oceans should include mineral compositions and iron contents of constituent minerals, as highlighted in the modeling study of iron

biogeochemical cycles conducted by Johnson and Meskhidze (2013). Mineral compositions and their iron chemistries were converted from world soil data for modeling (Claquin et al., 1999; Nikovic et al., 2012; Journet et al., 2014). However, a large degree of uncertainty remains regarding the mineralogical properties of fine particles in the source soils. In particular, data on the iron content of soil clay minerals are rarely available in the literature. Bulk and single-particle analyses of representative dust provide direct mineralogical information because soil particles lifted from wide source areas have been mixed thoroughly during long-range transport.

Our TEM analyses also revealed the mineralogical attributes of iron single dust particles. Iron was partitioned into (hydr)oxides and clay minerals. The iron (hydr)oxides were goethite and hematite, with minor contributions of magnetite. Their median volume contribution to the particles was ~1.5 vol%. Iron-bearing silicates are clay mineral aggregates dominated by ISCMs (Table 1). The average iron content of the clay mineral aggregates in Saharan dust particles is 5 wt%. Iron must be dissolved from clay minerals and iron (hydr)oxides before it is available for phytoplankton growth in the ocean (Rubin et al., 2011; Sholkovitz et al., 2012). The fractional Fe solubility (%Fe_S) of mineral dust (Sholkovitz et al., 2012) depends on iron content, crystallinity, and the specific surface areas of iron-bearing minerals (Lasaga, 1995; Nagy, 1995). The common nano-sized grains of ISCMs and iron (hydr)oxides with high specific surface areas and low crystallinity in the dust particles may enhance iron bioavailability (Baker and Jickells, 2006).

4. Summary and conclusions

Dust particles are composed of minerals with wide ranges of grain size and optical and chemical properties. The optical properties related to radiative forcing and remote sensing could be calculated optimally based on realistic mineralogical, morphological, and structural models of dust particles. Analysis of micronutrient delivery to remote oceans should consider the forms of the elements in the dust particles. TEM analysis of cross sections of dust particles, aided by EDXS, revealed the details of the internal mineralogical, structural, and morphological properties of fine Saharan dust particles. Saharan dust shares many properties with Asian dust, such as internal structure, mineral composition, and ISCM chemistry, but it differs slightly in its higher clay content, fewer pores, higher kaolinite content, and higher smectitic component in ISCMs. The overall 3D shapes of the dust particles were roughly ellipsoidal, with widely varying axial ratios. We emphasize, however, that this does not necessarily mean that their optical properties would match with those of corresponding ellipsoids. Rather, more likely, they do not (Lindqvist et al., 2014). Submicron grains of iron (hydr)oxides, mostly goethite and hematite, were commonly dispersed throughout the clay medium. Their median volume% was estimated at ~1.5%. Submicron- to nano-sized grains of ISCMs and iron (hydr)oxides would enhance the release of inorganic nutrients to ecosystems. These data on the mineralogical properties and structures of individual dust particles provide a basis for modeling optical properties of Saharan dust. However, we could not probe the interiors of coarse (> 10 μm) dust particles due to their low abundance in the probed dust plume and the technical difficulty of preparing large cross sections. Description of the general properties of single particles can be completed with coarse particle data

from further investigations.

Acknowledgements. This study was funded by the National Research Foundation of Korea grant NRF-2011-0028597 to G. Y. Jeong. K. Kandler greatly acknowledges support from the German Research Foundation (DFG, grants KA 2280/2 and FOR 539 SAMUM).

References

Anderson, J. R., Buseck, P. R., Patterson, T. L., and Arimoto, R.: Characterization of the Bermuda tropospheric aerosol by combined individual-particle and bulk-aerosol analysis, Atmos. Environ., 30, 319–338, 1996.

Arimoto, R., Zhang, X. Y., Huebert, B. J., Kang, C. H., Savoie, D. L., Prospero, J. M., Sage, S. K., Schoesslin, C. A., Khing, H. M., and Oh, S. N.: Chemical composition of atmospheric aerosols from Zhenbeitai, China, and Gosan, South Korea, during ACE-Asia, J. Geophys. Res., 109, D19S04, doi:10.1029/2003JD004323, 2004.

Avila, A., Queralt-Mitjans, I., and Alacón, M.: Mineralogical composition of African dust delivered by red rains over northeastern Spain, J. Geophys. Res., 102, D18, 21977–21996, ~~1996~~1997.

Baker, A. R. and Jickells, T. D.: Mineral particle size as a control on aerosol iron solubility, Geophys. Res. Lett., 33, L17608, doi:10.1029/2006GL026557, 2006.

Boyd, P. W., Watson, A. J., Law, C. S., Abraham, E. R., Trull, T., Murdoch, R., Bakker, D. C. E., Bowie, A. R., Buesseler, K. O., Chang, H., Charette, M., Croot, P., Downing, K., Frew, R., Gall, M., Hadfield, M., Hall, J., Harvey, M., Jameson, G., LaRoche, J., Liddicoat, M., Ling, R., Maldonado, M. T., McKay, R. M., Nodder, S., Pickmere, S., Pridmore, R., Rintoul, S., Safi, K., Sutton, P., Strzepek, R., Tanneberger, K., Turner, S., Waite, A., and Zeldis, J.: A mesoscale phytoplankton bloom in the polar Southern Ocean stimulated by iron fertilization, Nature, 407, 695–702, 2000.

Brindley, G. W.: Order-disorder in clay mineral structures, in: Crystal Structures of Clay Minerals and their X-ray Identification, edited by: Brindley, G. W., Goodman, G., 125–195, The Mineralogical Society, London, 1980.

Chiapello, I., Bergametti, G., Chatenet, B., Bousquet, P., Dulac, F., Soares, E.: Origins of African dust transported over the northeastern tropical Atlantic, J. Geophys. Res., 102 (D12), 13701–13709, doi:10.1029/97jd00259, 1997.

Conny, J. M.: Internal composition of atmospheric dust particles from focused ion-beam scanning electeron microscopy, Environ. Sci. Technol., 47, 8575–8581.

Coude-Gaussen, G., Rognon, P., Bergametti, G., Gomes, L., Strauss, B., Gros, J. M., and Le Coustumer, M. N.: Saharan dust on Fuerteventura Island (Canaries): Chemical and mineralogical characteristics, air mass trajectories, and probable sources, J. Geophys. Res.-Atmos., 92, 9753–9771, 1987.

Cwiertny, D. M., Young, M. A., and Grassian, V. H.: Chemistry and photochemistry of mineral dust aerosol,

Annu. Rev. Phys. Chem., 59, 27–51, 2008.

Deboudt, K., Gloter, A., Mussi, A., and Flament, P.: Red-ox speciation and mixing state of iron in individual African dust particles, J. Geophys. Res., 117, D12307, 10.1029/2011JD017298, 2012.

Dentener, F. J., Carmichael, G. R., Zhang, Y., Lelieveld, J., and Crutzen, P. J.: Role of mineral aerosol as a reactive surface in the global troposphere, J. Geophys. Res., 101, 22869–22889, 1996.

Dubovik, O., Sinyuk, A., Lapyonok, T., Holben, B. N., Mishchenko, M., Yang, P., Eck, T. F., Volten, H., Munoz, O., Veihelmann, B., van der Zande, W. J., Leon, J. F., Sorokin, M., and Slutsker, I.: Application of spheroid models to account for aerosol particle nonsphericity in remote sensing of desert dust, J. Geophys. Res.-Atmos., 111, D11208, doi:10.1029/2005JD006619, 2006.

Falkovich, A. H., Ganor, E., Levin, Z., Formenti, P., and Rudich, Y.: Chemical and mineralogical analysis of individual mineral dust particles, J. Geophys. Res.-Atmos., 106, 18029–18036, 2001.

Formenti, P., Schütz, L., Balkanski, Y., Desboeufs, K., Ebert, M., Kandler, K., Petzold, A., Scheuvens, D., Weinbruch, S., and Zhang, D.: Recent progress in understanding physical and chemical properties of African and Asian mineral dust, Atmos. Chem. Phys., 11, 8231–8256, doi:10.5194/acp-11-8231-2011, 2011.

Freedman, M.A.: Potential sites for ice nucleation on aluminosilicate clay minerals and related materials, The Journal of Physical Chemistry Letters, 6, 3850–3858, 2015.

Gao, Y., Anderson, J. R., and Hua, X.: Dust characteristics over the North Pacific observed through shipboard measurements during the ACE-Asia experiment, Atmos. Environ., 41, 7907–7922, 2007.

Glaccum, R. A. and Prospero, J. M.: Saharan aerosols over the tropical north Atlantic—Mineralogy, Mar. Geol., 37, 295– 321, 1980.

Jeong, G. Y.: The dependence of localized crystallization of halloysite and kaolinite on primary minerals in the weathering profile of granite, Clays Clay Miner., 48, 196–203, 2000.

Jeong, G. Y.: Bulk and single-particle mineralogy of Asian dust and a comparison with its source soils, J. Geophys. Res.-Atmos., 113, D02208, doi:10.1029/2007JD008606, 2008.

Jeong, G. Y. and Achterberg, E. P.: Chemistry and mineralogy of clay minerals in Asian and Saharan dusts and the implications for iron supply to the oceans, Atmos. Chem. Phys., 14, 12415–12428, 2014.

Jeong, G. Y. and Nousiainen, T.: TEM analysis of the internal structures and mineralogy of Asian dust particles and the implications for optical modeling, Atmos. Chem. Phys., 14, 7233–7254, 2014.

Jeong, G. Y., Yoon, H. I., and Lee, S. Y.: Chemistry and microstructures of clay particles in smectite-rich shelf sediments, South Shetland Islands, Antarctica, Mar. Geol., 209, 19–30, 2004.

Jeong, G. Y., Kim, J. Y., Seo, J., Kim, G. M., Jin, H. C., and Chun, Y.: Long-range transport of giant particles in Asian dust identified by physical, mineralogical, and meteorological analysis, Atmos. Chem. Phys., 14, 505–521, 2014.

Jickells, T. D., An, Z. S., Andersen, K. K., Baker, A. R., Bergametti, G., Brooks, N., Cao, J. J., Boyd, P. W., Duce, R. A., Hunter, K. A., Kawahata, H., Kubilay, N., laRoche, J., Liss, P. S., Mahowald, N., Prospero, J. M., Ridgwell, A. J., Tegen, I., and Torres, R.: Global Iron Connections Between Desert, Dust, Ocean Biogeochemistry, and Climate, Science, 308, 67–71, 2005.

Johnson, M. S., and Meskhidze, N.: Atmospheric dissolved iron deposition to the global oceans: effects of oxalate-promoted Fe dissolution, photochemical redox cycling, and dust mineralogy, Geosci. Model Dev., 6, 1137–1155, 2013.

Journet, E., Desboeufs, K. V., Caquineau, S., and Colin, J.-L.: Mineralogy as a critical factor of dust iron solubility, Geophys. Res. Lett. 35, L07805, doi:10.1029/2007GL031589, 2008.

Kahnert, M., Nousiainen, T., and Markkanen, J.: Morphological Models for Inhomogeneous Particles: Light scattering by aerosols, cometary dust, and living cells, Light Scattering Reviews, Vol 11, 2016 (in press).

Kanayama, S., Yabuki, S., Yanagisawa, F., and Motoyama, R.: The chemical and strontium isotope composition of atmospheric aerosols over Japan: the contribution of long-range-transported Asian dust (Kosa), Atmos. Environ., 36, 5159–5175, 2002.

Kandler, K., Benker, N., Bundke, U., Cuevas, E., Ebert, M., Knippertz, P., Rodríguez, S., Schütz, L., and Weinbruch, S.: Chemical composition and complex refractive index of Saharan Mineral Dust at Izaña, Tenerife (Spain) derived by electron microscopy, Atmos. Environ., 41, 8058–8074, 2007.

Kandler, K., Schütz, L., Deutscher, C., Ebert, M., Hofmann, H., Jäckel, S., Jaenicke, R., Knippertz, P., Lieke, K., Massling, A., Petzold, A., Schladitz, A., Weinzierl, B., Wiedensohler, A., Zorn, S., and Weinbruch, S.: Size distribution, mass concentration, chemical and mineralogical composition and derived optical parameters of the boundary layer aerosol at Tinfou, Morocco, during SAMUM 2006, Tellus, 61B, 32–50, 2009.

Kemppinen, O., Nousiainen, T., and Jeong, G. Y.: Effects of dust particle internal structure on light scattering, Atmos. Chem. Phys., 15, 12011 – 12027, 2015.

Klaver, A., Formenti, P., Caquineau, S., Chevaillier, S., Ausset, P., Calzolai, G., Osborne, S., Johnson, B., Harrison, M., and Dubovik, O.: Physico-chemical and optical properties of Sahelian and Saharan mineral dust: *in situ* measurements during the GERBILS campaign. Quarterly Journal of the Royal Meteorological Society, 137, 1193–1210, 2011.

Knippertz, P., Tesche, M., Heinold, B., Kandler, K., Toledano, C., and Esselborn, M.: Dust mobilization and aerosol transport from West Africa to Cape Verde–A meteorological overview of SAMUM-2, Tellus, 63B, 430–447, doi:10.1111/j.1600-0889.2011.00544.x, 2011.

Kulkarni, G. and Dobbie, S., Ice nucleation properties of mineral dust particles: determination of onset RHi , IN active fraction, nucleation time-lag, and the effect of active sites on contact angles, Atoms. Chem. Phys., 10, 95–105, 2010.

Lafon, S., Sokolik, I. N., Rajot, J. L., Caquineau, S., and Gaudichet, A.: Characterization of iron oxides in mineral dust aerosols: Implications for light absorption, *J. Geophys. Res.,* 111, D21207, doi:10.1029/2005JD007016, 2006.

Laskin, A., Wietsma, T. W., Krueger, B. J., and Grassian, V. H.: Heterogeneous Chemistry of Individual Mineral Dust Particles with Nitric Acid: A Combined CCSEM/EDX, ESEM, and ICP-MS Study, J. Geophys. Res.-Atmos., 110, D10208, 2005.

Lindqvist, H., Jokinen, O., Kandler, K., Scheuvens, D., and Nousiainen, T.: Single scattering by realistic, inhomogeneous mineral dust particles with stereogrammetric shapes, Atmos. Chem. Phys., 14, 143–157,

2014.

Mahowald, N. M., Engelstaedter, S., Luo, C., Sealy, A., Artaxo, P., Benitez-Nelson, C., Bonnet, S., Chen, Y., Chuang, P. Y., Cohen, D. D., Dulac, F., Herut, B., Johansen, A. M., Kubilay, N., Losno, R., Maenhaut, W., Paytan, A., Prospero, J. M., Shank, L. M., and Siefert, R. L.: Atmospheric iron deposition: global distribution, variability, and human perturbations. Annu. Rev. Mar. Sci., 1, 245–278, 2009.

Merikallio, S., Lindqvist, H., Nousiainen, T., and Kahnert, M.: Modelling light scattering by mineral dust using spheroids: assessment of applicability, Atmos. Chem. Phys., 11, 5347–5363, 2011.

Mishchenko, M.I., Travis, L.D., Kahn, R.A., and West, R.A.: Modeling phase functions for dustlike tropospheric aerosols using a shape mixture of randomly oriented polydisperse spheroids, J. Geophys. Res, 102, 16831–16847, 1997.

Nousiainen, T. and Kandler, K.: Light scattering by atmospheric mineral dust particles, Light Scattering Reviews, 9, 3–52, 2015.

Nousiainen, T. and Vermeulen, K.: Comparison of measured single-scattering matrix of feldspar particles with T - matrix simulations using spheroids. J. Quant. Spectrosc. Radiat. Transfer, 79–80, 1031–1042, 2003.

Okada, K., Naruse, H., Tanaka, T., Nemoto, O., Iwasaka, Y., Wu, P. -M., Ono, A., Duce, R. A., Uematsu, M., Merrill, J. T., and Arao, K.: X-ray spectrometry of individual Asian dust-strom particles over the Japanese islands and the north Pacific Ocean, Atmos. Environ., 24A, 1369–1378, 1990.

Okada, K., Heintzenberg, J., Kai, K., and Qin, Y.: Shape of atmospheric mineral particles collected in three Chinese arid-regions, Geophysical Research Letter, 28, 3123–3126, 2001.

Ooki, A. and Uematsu, M.: Chemical interactions between mineral dust particles and acid gases during Asian dust events, J. Geophys. Res., 110, D03201, doi:10.1029/2004JD004737, 2005.

Park, M. Y. and Jeong, G. Y.: Mineralogical properties of Asian dust sampled at Deokjeok Island, Incheon, Korea in February 22, 2015, J. Min. Soc. Korea, 29, 79–87, 2016.

Reid, J. S., Jonsson, H. H., Maring, H. B., Smirnov, A., Savoie, D. L., Cliff, S. S., Reid, E. A., Livingston, J. M., Meier, M. M., Dubovik, O., and Tsay, S. C.: Comparison of size and morphological measurements of coarse mode dust particles from Africa, J. Geophys. Res., 108, doi:10.1029/2002JD002485, 2003.

Ro, C. -U., Hwang, H., Kim, H., Chun, Y., and Van Grieken, R.: Single-particle characterization of four ‘‘Asian dust’’ samples collected in Korea, using low-Z particle electron probe X-ray microanalysis, Environ. Sci. Technol., 39, 1409–1419, 2005.

Rubin, M., Berman-Frank, I., and Shaked, Y.: Dust- and mineral iron utilization by the marine dinitrogen-fixer *Trichodesmium*, Nat. Geosci., 4, 529–534, doi:10.1038/NGEO1181, 2011.

Scheuvens, D., Schütz, L., Kandler, K., Ebert, M., Weinbruch, S.: Bulk composition of northern African dust and its source sediments — A compilation, Earth-Science Reviews, 116, 170–194, 2013.

Seinfeld, J. H., Carmichael, G. R., Arimoto, R., Conant, W. C., Brechtel, F. J., Bates, T. S., Cahill, T. A., Clarke, A. D., Doherty, S. J., Flatau, P. J., Huebert, B. J., Kim, J., Markowicz, K. M., Quinn, P. K., Russell, L. M., Russell, P. B., Shimizu, A., Shinozuka, Y., Song, C. H., Tang, Y., Uno, I., Vogelmann, A. M., Weber, R. J., Woo, J. -H, and Zhang, X. Y.: ACE-ASIA regional climatic and atmospheric chemical effects of Asian dust

and pollution, B. Am. Meteorol. Soc., 85, 367–380, 2004.

Shao, L., Li, W., Xiao, Z., and Sun, Z.: The mineralogy and possible sources of spring dust particles over Beijing, Adv. Atmos. Sci., 25, 395–403.

Shi, Z., Shao, L., Jones, T.P., and Lu, S.: Microscopy and mineralogy of airborne particles collected during severe dust storm episodes in Beijing, China, J. Geophys. Res., 110, D01303, doi:10.1029/2004JD005073, 2005.

Sokolik, I. N., Toon, O. B.: Direct radiative forcing by anthropogenic airborne mineral aerosols, Nature, 381, 681–683, 1996.

Stein, A. F., Draxler, R. R., Rolph, G. D., Stunder, B. J. B., Cohen, M. D., Ngan, F.–: NOAA's HYSPLIT Atmospheric Transport and Dispersion Modeling System, Bull. Am. Met. Soc. 96, 2059–2077, doi: 10.1175/bams-d-14-00110.1, 2015.

Swap, R., Garstang, M., Greco, S., Talbot, R., Kållberg, P.: Saharan dust in the Amazon Basin, Tellus, 44B, 133–149, 1992.

Tegen, I., and Lacis, A. A.: Modeling of particle size distribution and its influence on the radiative properties of mineral dust aerosol, J. Geophys. Res., 101, 19237–19244, 1996.

Vepraskas, M. J., and Wilson, M. A.: Soil Micromorphology: concepts, techniques, and applications, in: Methods of Soil Analysis, Part 5, edited by: Ulery, A. L., Dress, L. R., Soil Science Society of America Book Ser. 5, 191–226, Soil Science Society of America, Madison, Wisconsin, 2008.

Table 1. Mineral number % of Saharan dust based on SEM-EDXS analyses of single particles.

Size	No. of particle	Total clay minerals	ISCMs*	Ka	Ch	Bt	Q	P	Kf	Am	Ca	D	Fe	Ti	Gy	Sp	Ap
Saharan dust, Tenerife (This study)																	
0.9-2.5 μm	*n*=1191	1005	868	131	6	0	105	21	17	1	12	5	8	8	9	0	0
	%	84.4	72.9	11.0	0.5	0.0	8.8	1.8	1.4	0.1	1.0	0.4	0.7	0.7	0.8	0.0	0.0
> 2.5 μm	*n*=435	314	260	45	8	1	59	23	17	1	9	1	3	2	4	1	1
	%	72.7	60.2	10.4	1.9	0.2	13.7	5.3	3.9	0.2	2.1	0.2	0.7	0.5	0.9	0.2	0.2
Total	*n*=1626	1319	1128	176	14	1	164	44	34	2	21	6	11	10	13	1	1
	%	81.1	69.4	10.8	0.9	0.1	10.1	2.7	2.1	0.1	1.3	0.4	0.7	0.6	0.8	0.1	0.1
Asian dust, Korea (Jeong and Achterberg, 2014)**																	
%		56.1	48.4	1.8	3.9	2.1	18.7	10.5	4.0	0.7	6.5	1.0	1.2	0.2	0.8	0.2	0.2

*ISCM=illite-smectite series clay minerals, Ka=kaolinite, Ch=chlorite, Bt=biotite, Q=quartz, P=plagioclase, Kf=K-feldspar, Am=amphibole, Ca=calcite, D=dolomite, Fe=iron (hydr)oxide, Ti=Ti oxide, Gy=gypsum, Sp=sphene, Ap=apatite.

** Average value of the SEM-EDXS results from three Asian dust samples presented in Jeong and Achterberg (2014). Vaules are slightly differernt from those in Jeong and Achterberg (2014) by the change of mineral species considered for quantification.

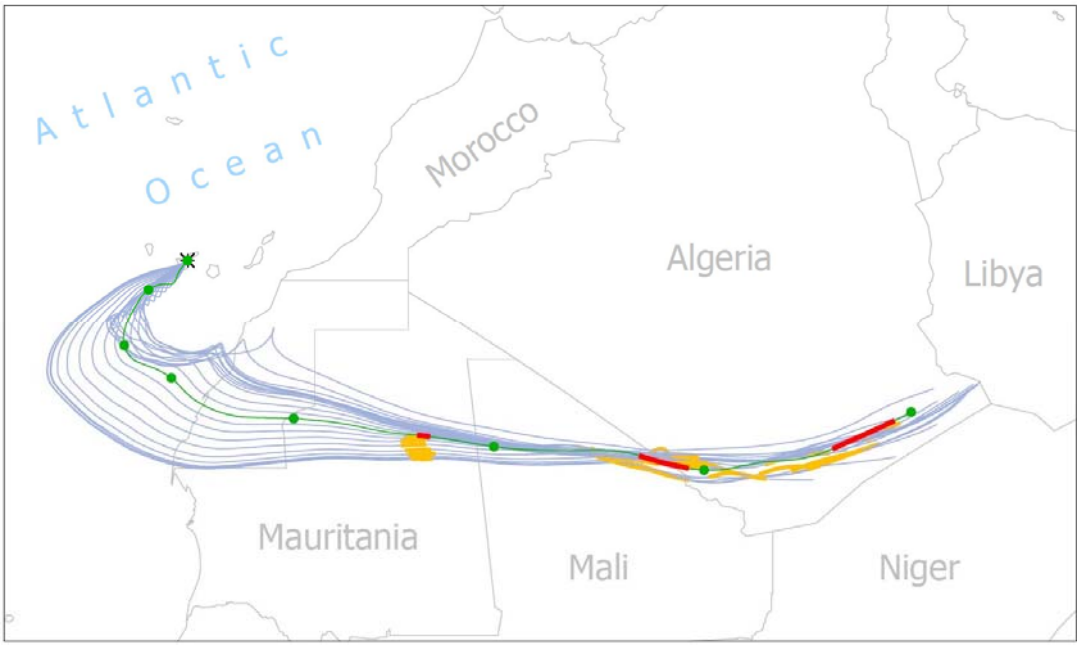

Figure 1. Map of northwestern Africa with the hourly 168-h backward trajectory evolution, which shows dust arriving at Izaña (2400 m asl.) on 16 July 2005. Green trajectories represent the impactor sample. The filled circles indicate 24-h periods. Trajectory sections where the altitude is below the mixing layer height are enhanced in orange/red.

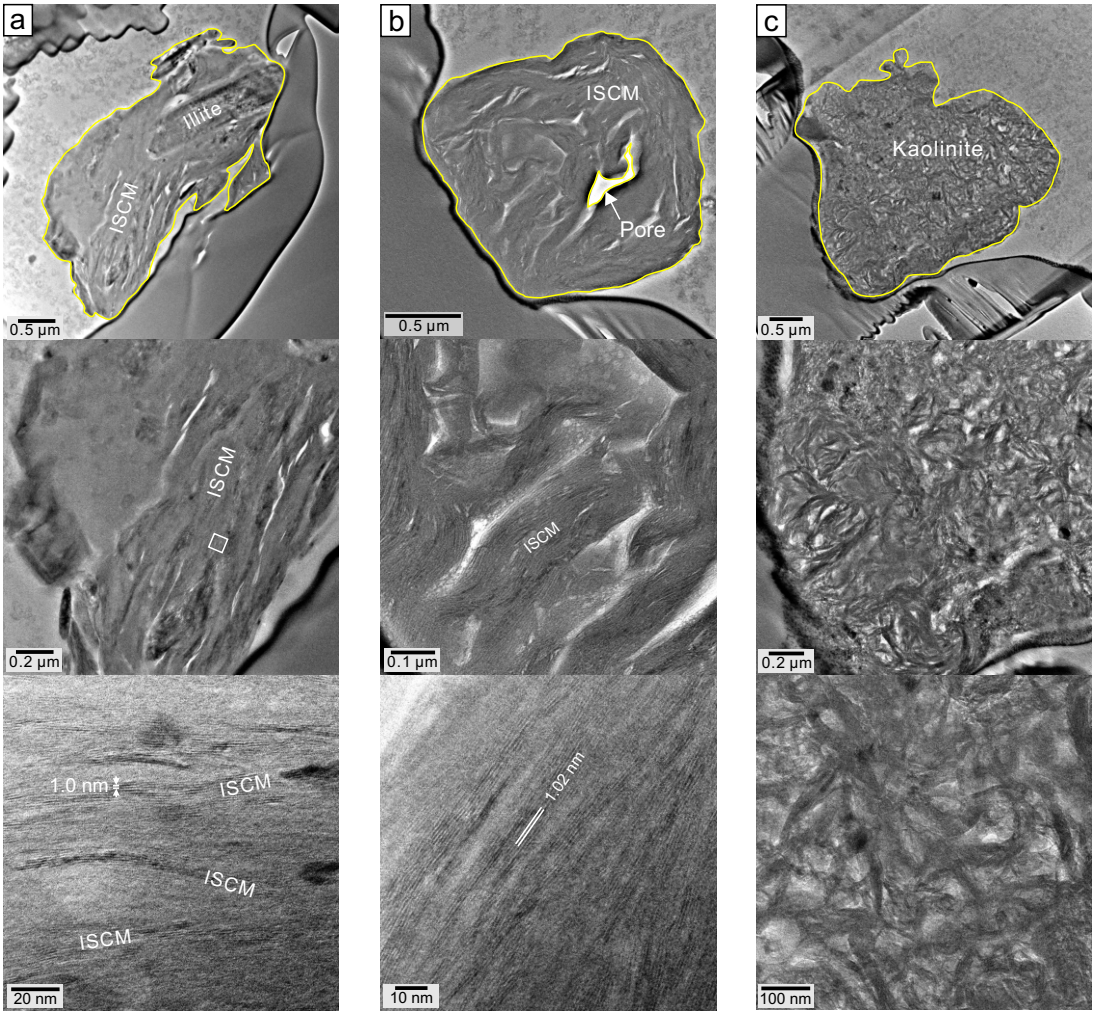

Figure 2. TEM images of cross sections of clay-rich dust particles. ISCM: illite–smectite series clay minerals, including illite, smectite, and their mixed layers. (a) ISCM clays, including an illite grain (particle 30). (b) ISCM clay (particle 48). (c) Kaolinite (particle 40). Yellow lines were added to show the boundary of particle and pore.